H-alpha Kinematics of the SINGS Nearby Galaxies Survey. I

O. Daigle, C. Carignan, P. Amram, O. Hernandez, L. Chemin, C. Balkowski, R. Kennicutt

Hα kinematics of the SINGS nearby galaxies survey – I[★]

O. Daigle,[1]† C. Carignan,[1] P. Amram,[2] O. Hernandez,[1,2] L. Chemin,[1]
C. Balkowski[3] and R. Kennicutt[4]

[1]*Observatoire du mont Mégantic, LAE, Université de Montréal, C. P. 6128 succ. centre ville, Montréal, Québec, H3C 3J7, Canada*
[2]*Observatoire Astronomique de Marseille Provence, Laboratoire d'Astrophysique de Marseille, 2 place Le Verrier, F-13248 Marseille Cedex 04, France*
[3]*Observatoire de Paris, section Meudon, GEPI, CNRS UMR 8111 et Universit é Paris 7, 5 place J. Janssen, 92195 Meudon Cedex, France*
[4]*Department of Astronomy, Steward Observatory, 933 N. Cherry Ave., Tucson, AZ 85721-0065, USA*

ABSTRACT

This is the first part of an Hα kinematics follow-up survey of the *Spitzer* Infrared Nearby Galaxies Survey (SINGS) sample. The data for 28 galaxies are presented. The observations were done on three different telescopes with Fabry–Perot of New Technology for the Observatoire du mont Megantic (FaNTOmM), an integral field photon-counting spectrometer, installed in the respective focal reducer of each telescope. The data reduction was done through a newly built pipeline with the aim of producing the most homogenous data set possible. Adaptive spatial binning was applied to the data cubes in order to get a constant signal-to-noise ratio across the field of view. Radial velocity and monochromatic maps were generated using a new algorithm, and the kinematical parameters were derived using tilted-ring models.

Key words: methods: observational. – techniques: radial velocities – galaxies: kinematics and dynamics.

1 INTRODUCTION

The Legacy survey *Spitzer* Infrared Nearby Galaxies Survey (SINGS) wants to characterize the infrared (IR) emission across the entire range of galaxy properties and star formation environments, including regions that until now have been inaccessible at IR wavelengths (Kennicutt et al. 2003). SINGS will provide:

(i) new insights into the physical processes connecting star formation to the interstellar medium (ISM) properties of galaxies;
(ii) a vital foundation of data, diagnostic tools and astrophysical inputs for understanding *Spitzer* observations of the distant Universe and ultraluminous and active galaxies;
(iii) an archive that integrates visible/ultraviolet (UV) and IR/submillimetre studies into a coherent self-consistent whole, and enables many follow-up investigations of star formation and ISM.

The *Spitzer* observations will provide images in seven different bands from 3.6 to 160 μm and spectroscopic data at medium and low resolution in the range 5–95 μm. These data will be used to trace the distribution and content of different dust components, from the polycyclic aromatic hydrocarbons (PAHs) and very small grains in

the mid-IR to the big grains in the far-IR (FIR; del Burgo et al. 2003; Kennicutt et al. 2003). Ancillary, multiwavelength observations will provide images in X-rays, UV (1300–2800 Å imaging and spectrophotometry), *BVRIJHK*, Hα, Paα, FIR, submillimetre, CO and H I. A total of 20 ground- and space-based telescopes are providing supporting data.

These data will help understand the process of star formation and feedback mechanisms that are fundamental parameters regulating the formation and evolution of galaxies. History of star formation has been strongly different for galaxies of different morphological type and luminosity. While short events of star formation, probably triggered by violent merging, formed most stars in elliptical galaxies, late-type systems seem to have their star formation modulated by the angular momentum (Sandage 1986) or by the mass of the initial system (Boselli 2001). Thus, the process of star formation and feedback must be clearly understood in order to understand galaxies' evolution. However, these physical processes are still poorly known. The primordial atomic gas has to condense into molecular clouds to form stars. The newly formed stars inject metals into the ISM via stellar winds, heat the dust and ionize the surrounding gas. It seems that the activity of star formation is regulated by the total gas surface density (Kennicutt 1989), but the role of rotation in this process is still unclear.

Even as important as it seems, no gathering of optical kinematical data was planned for the SINGS galaxies. This paper, by providing the Hα kinematics over the whole optical extent for 28 galaxies of the SINGS sample, wants to make up for this lack. A total of 58 SINGS galaxies are potentially observable in the Hα emission line

(see Section 2.1). The Hα kinematics of the 30 remaining galaxies of the observable part of the sample will be published in a forthcoming paper. These data were obtained with Fabry–Perot of New Technology for the Observatoire du mont Megantic (FaNTOmM) on three different telescopes (see Section 2.3). FaNTOmM is an integral field spectrometer made of a photon-counting camera using a third-generation photocathode, a scanning Fabry–Perot (FP) and a narrow-band interference filter. FaNTOmM was coupled to the focal reducer of the telescopes used. The photocathode used has a high quantum efficiency (∼30 per cent at Hα). This camera enables one to rapidly scan (∼5–10 min) the FP Free Spectral Range (FSR) and to cycle many times during an observation, thus averaging changing photometric conditions, as compared to CCD observations where scanning must be done slowly to overcome the readout noise [details about the camera can be found in Hernandez et al. (2003) and Gach et al. (2002)]. In this paper, Section 2 gives an overview of the observational campaign and of the galaxies studied. Section 3 discusses how the data were reduced, processed, and how the kinematical data and parameters were extracted. Section 4 provides all the maps extracted from the work done in Section 3. Section 5 discusses the advantages of FP kinematical data as compared to other kinematical data. A short appendix is added to comment the observational characteristics of the galaxies presented. Once completed, the data set will be available in the SINGS data base, as for the other SINGS ancillary surveys.

2 OBSERVATIONS

2.1 The sample

The SINGS sample, as defined by Kennicutt et al. (2003), is composed of 75 nearby ($\Delta < 30$ Mpc, median of 9.5 Mpc, for $H_0 = 70$ km s^{-1} Mpc^{-1}) galaxies, covering a wide range in a 3D parameter space of physical properties:

(i) morphological type (E to Im), which is also correlated with the star formation rate (SFR) per unit mass, gas fraction and bulge/disc ratio;

(ii) luminosity (IR quiescent to luminous IR galaxies), which is also correlated with galaxy mass, internal velocity and mean metallicity;

(iii) FIR/optical ratio covering over 3 orders of magnitude, which is also correlated with dust optical depth, dust temperature and inclination.

Roughly 12 galaxies were chosen in each RC3 type (E–S0, Sa–Sab, Sb–Sbc, Sc–Scd, Sd–Sm and Im–I0) which allows the coverage of a full combination of luminosity and IR/optical ratio [$5 \times 10^5 \, L_\odot < L_V < 2 \times 10^{11} \, L_\odot$, $10^7 \, L_\odot < L(\mathrm{IR}) < 10^{11} \, L_\odot$ and $0.02 < L(\mathrm{IR})/L_R < 42$]. Care was also taken to choose galaxies covering a wide range of other properties, such as nuclear activity, inclination, surface brightness, CO/H I ratio, bar structure, spiral arm structure, isolated/interacting, group members, cluster members. Galaxies lying far from the Galactic plane were preferred to avoid a high density of foreground stars and galactic extinction.

From the 75 galaxies of the sample, only those which present H II regions (star formation regions) can be observed in Hα in order to map their kinematics. Mainly, most early-type galaxies (E to S0–Sa) lack Hα emission and could not be observed. Starting from Sb galaxies, it is usually possible to extract the Hα kinematics. Fig. 1 shows the morphological type distribution of the presented galaxies and highlights the observational bias caused by the lack of
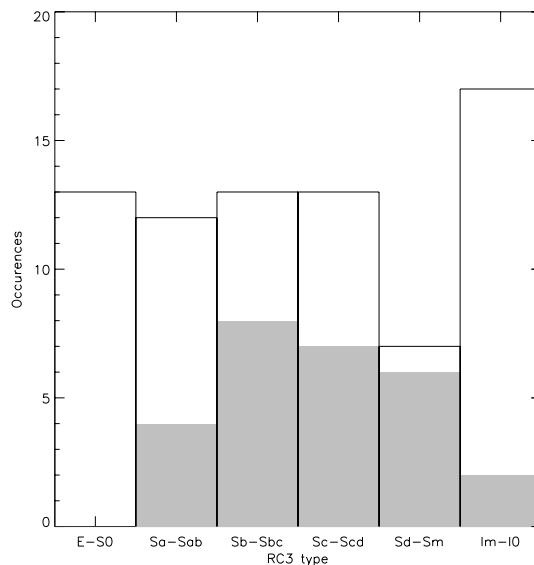

Figure 1. The SINGS RC3 galaxy type distribution. The grey area shows the galaxies presented in this paper.

Hα emission in early-type galaxies. Also, Im–I0 galaxies are usually very small and could not be observed on the 1.6-m telescope at the Observatoire du mont Mégantic. These galaxies need a 4-m class telescope to be observed. The velocity maps and the observed galaxies' positions are shown in Fig. 2. This figure also shows the relative sizes of the galaxies (in kpc). The basic galaxy parameters are presented in Table 1. Table 2 gives the observation conditions and information for each galaxy.

2.2 The hardware

All the observations were made with the integral field spectrometer, FaNTOmM. It consists of a narrow-band (typically 15 Å) interference filter, a FP interferometer and a photon-counting camera, used as the imaging device. FaNTOmM is coupled to the respective focal reducer of the telescopes on to which it is attached. The focal reducer PANORAMIX is used at the 1.6-m telescope of the Observatoire du mont Mégantic (OMM), CIGALE at the European Southern Observatory (ESO; La Silla) 3.6-m telescope and MOS/FP at the Canada–France–Hawaii 3.6-m Telescope (CFHT). The effective focal ratio, pixel size and field of view are summarized in Table 3. Interestingly, the pixel size obtained at the OMM (1.6 arcsec), where most of the galaxies were observed, is a close match to the one achieved by the *Spitzer*'s Infrared Array Camera (better than 2 arcsec, in the 3.6–8 μm range). This is, however, pure coincidence.

The interference filter is used to 'select' the radial velocity range that will be observed. It is chosen to allow only the galaxy's Hα emission to pass through. Since most galaxies' radial velocities span a maximum of $\pm 250 \sin i$ km s^{-1}, a maximum Doppler shift of ± 5.5 Å is expected around the galaxy's redshifted emission. The interference filter used must allow this emission to pass through whilst being as narrow as possible to avoid too much sky background emission from reaching the detector. A collection of 23 filters having a full width at half-maximum (FWHM) of ∼15 Å, covering the red spectrum from 6565 to 6785 Å in steps of 10 Å, was used to observe the galaxies in the sample. This set of filters allows galaxies with -300 km s$^{-1} \lesssim v_{\mathrm{sys}} \lesssim 10\,000$ km s^{-1} to be observed. Fig. 3 shows a
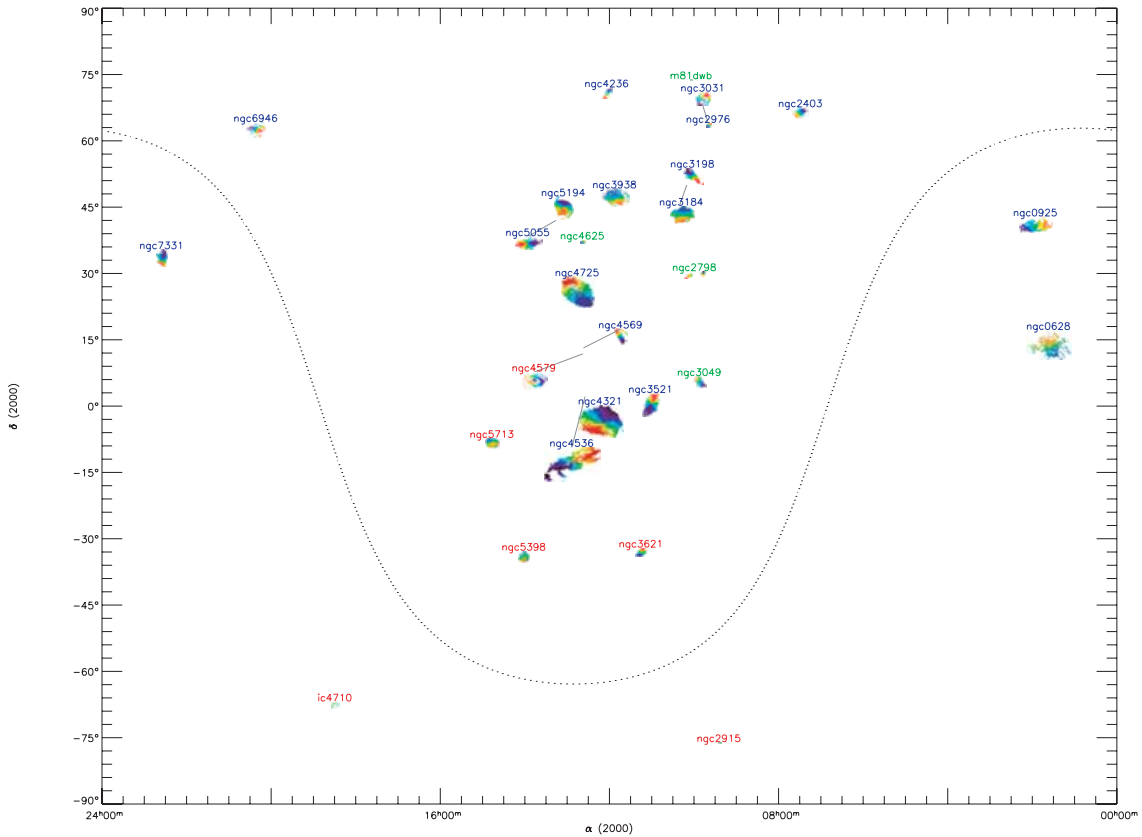
Figure 2. The SINGS Hα kinematics sky coverage so far. The names in blue correspond to the observations done at the OMM, in green at the CFHT and in red at the ESO 3.6-m telescope. Galaxies' relative sizes are to scale. The galactic equator is shown as the dotted line. Naturally, there is a strong concentration towards the Virgo cluster.

typical filter used for the observations. Centred at ∼6598 Å, it has a FWHM of 18 Å. By tilting the filter by a couple of degrees, it is possible to blueshift its central wavelength by a few Å to allow the filter to be exactly centred on the galaxy's rest Hα emission. The filters must also be chosen according to the expected outdoor temperature as they are typically blueshifted as temperature goes down. This shift is of the order of $-0.2\,\text{Å}\,\text{K}^{-1}$. As filters age, they also tend to blueshift. They must be scanned regularly to keep a good knowledge of their characteristics.

The FP interferometer is chosen to allow most of the Hα emission of the galaxy to be visible in a single FSR. The interference orders of the FP interferometers used vary from $p = 609$ (FSR = 10.93 Å) to $p = 899$ (FSR = 7.3 Å) at rest Hα. Another parameter that has to be taken into account is the FP *Finesse*. The Finesse, F, is a dimensionless value expressing the spectral resolution, R, of the etalon such as

$$R = \frac{F\lambda_0}{\text{FSR}} = \frac{\Delta\lambda}{\lambda}$$

and

$$\text{FSR} = \frac{\lambda_0}{p}.$$

To properly sample the light that comes out of the FP, the number of channels scanned must be at least 2.2 times (Nyquist) the Finesse. Many different factors affect the Finesse: the reflectivity of the reflecting plates of the FP, the optical and mechanical properties of the

surfaces (usually polished to $< \frac{\lambda}{100}$), the temperature, the humidity and the observational setup (the parallelism, the accuracy of the focus of the focal reducer). In fact, the environmental effects and the observational setup should not affect the Finesse, but, as shown in Table 4, the scatter in Finesses obtained must be explained by these phenomena. Finesses achieved for the observations presented in this paper range from 8 to 20. A total of three different FP etalons were used for the observations. The interference filter and PF interferometer must be chosen so that no more that three FSRs of the etalon pass through the filter, as shown in Fig. 3.

The photon-counting camera used for this survey is based on a GaAs Hamamatsu photocathode coupled with a Dalsa commercial CCD. The photocathode has a quantum efficiency of ∼28 per cent at Hα, and the CCD has 1024×1024 12.5 µm square pixels. The CCD was operated in its low spatial resolution mode, where pixels are binned 2×2, and at a frame rate of 40 frames per second. The effective pixel sizes on the sky are given in Table 3. The photon-counting camera is an essential tool to achieve such a survey. Its ability to rapidly scan the FP interferometer allows the photometric conditions' variations to be averaged out. For comparison, in CCD observations, each FP channel must be observed for at least five contiguous minutes to make sure that the read-out noise of the CCD does not mask the weak galaxy's signal. This means that photometric conditions must not significantly change for ∼4 h with CCD observations (given that 48 FP channels are scanned). In photon counting, channels are observed for 5–15 s, and cycles are

Table 1. Observational data for the SINGS Hα kinematics sample.

Galaxy name	α(J2000) (hh mm ss)	δ(J2000) ($°\,'\,''$)	Type RC3	Δ^a (Mpc)	$D_{25}^{b,i}\ ^b$ (arcmin)	$B_T^{b,i}\ ^c$	$M_B^{b,i}\ ^d$	Systemic velocity^e (km s^{-1})
NGC 628	01 36 41.8	+15 47 00	SA(s)c	11.4	10.5 × 9.5	9.95	−20.33	657
NGC 925	02 27 16.8	+33 34 41	SAB(s)d	9.3	11.2	10.6	−19.24	554
NGC 2403	07 36 54.5	+65 35 58	SAB(s)cd	4.2	21.4	8.5	−19.61	132
NGC 2798	09 17 22.9	+41 59 59	SB(s)a pec	24.7	2.6 × 1	13.04	−18.92	1726
NGC 2915	09 26 11.5	−76 37 35	I0	2.7	1.9 × 1	13.25	−13.91	468
NGC 2976	09 47 15.4	+67 54 59	SAc pec	3.5	5.9 × 2.7	10.82	−16.90	3
NGC 3049	09 54 49.6	+09 16 18	SB(rs)ab	19.6	2.2 × 1.4	13.04	−18.42	1494
NGC 3031	09 55 33.2	+69 03 55	SA(s)ab	3.5	26.9 × 14.1	7.89	−19.83	−34
UGC 5423	10 05 30.6	+70 21 52	Im	3.5	0.9 × 0.6	15.19	−12.53	350
NGC 3184	10 18 17.0	+41 25 28	SAB(rs)cd	8.6	7.4 × 6.9	10.36	−19.31	592
NGC 3198	10 19 54.9	+45 33 09	SB(rs)c	14.5	7.8	11.1	−19.70	660
NGC 3521	11 05 48.6	−00 02 09	SAB(rs)bc	9	11 × 5.1	9.83	−19.94	805
NGC 3621	11 18 16.3	−32 48 45	SA(s)d	6.2	12.3 × 7.1	10.28	−18.68	727
NGC 3938	11 52 49.4	+44 07 15	SA(s)c	12.2	5.4 × 4.9	10.90	−19.53	809
NGC 4236	12 16 42.1	+69 27 45	SB(s)dm	2.2	16.4	9.5	−17.21	2
NGC 4321	12 22 55.2	+15 49 23	SAB(s)b	16.1	7.4	10.0	−21.03	1590
NGC 4536	12 34 27.1	+02 11 16	SAB(rs)bc	25	7.6 × 3.2	11.16	−20.82	1808
NGC 4569	12 36 49.8	+13 09 46	SAB(rs)ab	20	9.5 × 4.0	10.26	−21.24	−235
NGC 4579	12 37 43.6	+11 49 05	SAB(rs)b	20	5.9 × 4.7	10.48	−21.18	1591
NGC 4625	12 41 52.7	+41 16 25	SAB(rs)m pec	9.5	2.2 × 1.9	12.92	−16.97	609
NGC 4725	12 50 26.6	+25 30 06	SAB(r)ab pec	17.1	10.7 × 7.6	10.11	−21.05	1206
NGC 5055	13 15 49.3	+42 01 45	SA(rs)bc	8.2	12.6 × 7.2	9.31	−20.26	504
NGC 5194	13 29 52.7	+47 11 43	SA(s)bc pec	8.2	11.2 × 6.9	8.96	−20.61	463
NGC 5398	14 01 21.5	−33 03 50	SB(rs)dm	15	2.8 × 1.7	12.78	−18.10	1216
NGC 5713	14 40 11.5	−00 17 21	SAB(rs)bc pec	26.6	2.8 × 2.5	11.84	−20.28	1883
IC 4710	18 28 38.0	−66 58 56	SB(s)m	8.5	3.6 × 2.8	12.5	−17.14	741
NGC 6946	20 34 52.0	+60 09 15	SAB(rs)cd	5.5	14.9	7.92	−20.78	46
NGC 7331	22 37 04.1	+34 24 56	SA(s)b	15.7	10.5 × 3.7	10.35	−20.63	816

^{a} Δ: distance in Mpc, flow corrected for $H_0 = 70$ km s^{-1} Mpc^{-1}, as presented in Kennicutt et al. (2003).
^{b} $D_{25}^{b,i}$: optical diameter at the 25 mag arcsec^{-2} in B, corrected for the effects of projection and extinction. Taken from the RC3.
^{c} $B_T^{b,i}$: corrected total apparent magnitude in B. Taken from the RC3.
^{d} $M_B^{b,i}$: corrected total absolute magnitude in B. Calculated from Δ and $B_T^{b,i}$.
^{e} Systemic velocity: galaxy's systemic velocity. Taken from Kennicutt et al. (2003).

looped every 4–15 min. Many cycles are made during an observation. Signal-to-noise ratio (SNR) estimations can be made throughout the observations, and the observer can decide when to stop the integration. Since the calibration lamp is pretty strong as compared to galaxies' fluxes, the calibrations are done in analogue mode (non-photon counting). Typically, calibration channels are integrated 1 s each.

2.3 Observing runs

The observations of the sample presented here were spread over 10 observing runs taking place in the last 2 yr. Eight runs took place at the Observatoire du mont Megantic 1.6-m telescope (OMM), where FaNTOmM is a permanent instrument. FaNTOmM was taken to the CFHT and the ESO 3.6-m telescope (ESO/La Silla) as a visitor instrument for the other two runs of this survey. The large field of view available at the OMM permitted the observation of large galaxies (NGC 5194, NGC 3031,...) in one single field. Smaller galaxies visible in the Northern hemisphere were observed at the CFHT. A single observing run took place in the southern hemisphere on the ESO/La Silla telescope in 2004 April. Few galaxies of the SINGSsurvey were visible at that time, resulting in a poor coverage of galaxies at negative declinations.

3 DATA REDUCTION

Raw observational data consist of many data files that contain photons' positions for every cycle/channel duo. If cycling is done with, say, 15 s per channel integration time, one file is created every 15 s. Data reduction consists of the following steps.

(i) Integration of the raw data files into an interferogram data cube (3D data cube sliced for every FP channel);
(ii) phase correction of the interferograms to create wavelength-sorted data cubes (3D data cube sliced for every wavelength interval);
(iii) hanning spectral smoothing;
(iv) sky emission removal;
(v) spatial binning/smoothing;
(vi) extraction of radial velocity maps from emission-line positions;
(vii) addition of the astrometric information (World Coordinate System information) to the data files;
(viii) kinematical information extraction.

All the reduction was performed with IDL routines inspired by the ADHOCW reduction package (http://www-obs.cnrs-mrs.fr/adhoc/adhoc.html), except for the last two steps, in which cases third-party software was used (see respective sections for more details). The IDL reduction package was written to allow more

Table 2. Journal of the Fabry–Perot observations.

Galaxy name	Date	Filter			Effective integration			Fabry–Perot			Sampling	
		$\lambda_c{}^d$ (Å)	FWHM^e (Å)	$T_{max}{}^f$ (per cent)	$t_{exp}{}^g$ (min)	$t_{Channel}{}^h$ (min)	p^i	FSR^j (km s^{-1})	F^k	R^l	NCH^m	STP^n (Å)
NGC 628^a	2003/11/18	6598	18.2	73	149	2.33	899	333.47	23.6	21216	64	0.11
NGC 925^a	2002/02/11	6584	15	75	132	2.75	765	391.88	16	12240	48	0.18
NGC 2403^a	2002/11/17	6569	10	50	120	3.00	765	391.88	14	10710	40	0.21
NGC 2798^b	2003/04/04	6608	16.2	69	96	2.00	899	333.47	16	14384	48	0.15
NGC 2915^c	2004/21/04	6581	19.8	60	149	4.67	609	492.27	14.3	8580	32	0.34
NGC 2976^a	2003/01/30	6581	19.8	60	184	3.83	899	333.47	16.5	14834	48	0.15
NGC 3049^b	2003/04/08	6598	18.2	73	144	3.00	899	333.47	17.4	15643	48	0.15
NGC 3031^a	2003/02/06	6581	19.8	60	272	5.55	899	333.47	14.3	12856	48	0.15
UGC 5423^b	2003/04/06	6565	15	40	120	2.50	899	333.47	18.5	16632	48	0.15
NGC 3184^a	2004/02/18	6584	15.5	74	162	3.37	765	391.88	17.6	13464	48	0.18
NGC 3198^a	2003/03/06	6584	15.5	74	260	5.00	899	333.47	23	20976	52	0.14
NGC 3521^a	2004/02/19	6584	15.5	74	120	2.50	765	391.88	16.0	12240	48	0.18
NGC 3621^c	2004/20/04	6584	15.5	74	128	4.00	609	492.27	14.4	8640	32	0.34
NGC 3938^a	2004/03/11	6584	15.5	74	128	2.66	765	391.88	16.8	12852	48	0.18
NGC 4236^a	2004/02/27	6581	19.8	60	182	3.50	899	333.47	23	20977	52	0.14
NGC 4321^a	2003/02/25	6608	16.2	69	260	5.00	899	333.47	23	20977	52	0.14
NGC 4536^a	2004/03/14	6598	18.2	73	163	3.40	765	391.88	21.3	16295	48	0.18
NGC 4569^a	2002/03/11	6569	15.0	60	152	3.80	765	391.88	20.5	15682	40	0.21
NGC 4579^a	2002/04/04	6598	10.0	60	92	2.30	609	492.27	19.6	14494	40	0.27
NGC 4625^b	2003/04/06	6581	19.8	60	120	2.50	899	333.47	15.9	14294	48	0.15
NGC 4725^a	2004/02/19	6584	15.5	74	120	2.50	765	391.88	18.7	14305	48	0.18
NGC 5055^a	2004/03/14	6584	15.5	74	128	2.66	765	391.88	16.8	12852	48	0.18
NGC 5194^a	2003/05/18	6581	19.8	60	246	5.14	899	333.47	20.7	18609	48	0.15
NGC 5398^c	2004/10/04	6598	18.2	73	149	4.66	609	492.27	12.0	7308	32	0.34
NGC 5713^c	2004/13/04	6608	16.2	69	150	6.25	609	492.27	9.5	5785	24	0.45
IC 4710^c	2004/15/04	6598	18.2	73	48	2.00	609	492.27	8.8	5359	24	0.45
NGC 6946^a	2000/11/19	6569	10	50	120	2.00	765	391.88	14	10710	40	0.21
NGC 7331^a	2002/11/03	6584	15.5	74	174	3.62	765	391.88	15.9	12164	48	0.18

^{a}OMM: Observatoire du mont Mégantic, Québec, Canada. 1.6-m telescope.

^{b}CFHT: Canada–France–Hawaii Telescope, Hawaii, USA. 3.6-m telescope.

^{c}ESO: European Southern Observatory, La Silla, Chile. 3.6-m telescope.

$^d\lambda_c$: non-tilted filter central wavelength at 20°C.

^{e}FWHM: non-tilted filter Full Width Half Maximum at 20°C.

$^f T_{max}$: non-tilted filter maximum transmission at λ_c and at 20°C.

$^g t_{exp}$: total effective exposure time in minutes (total exposure time × mean counting efficiency).

$^h t_{channel}$: total effective exposure time per channel in minutes (total exposure time per channel × mean counting efficiency).

^{i}p: FP interference order at Hα.

^{j}FSR: FP Free Spectral Range at Hα in km s^{-1}.

^{k}F: mean Finesse through the field of view.

^{l}R: spectral resolution ($\Delta\lambda/\lambda$) according to the computed *Finesse*.

^{m}NCH: number of channels done by cycle in multiplex observations.

^{n}STP: wavelength step in Å.

flexibility of the data reduction, such as telescope guiding error correction, better removal of the sky background emission through sky cube fitting and stronger emission-line barycentre determination algorithm. The newly introduced reduction routines are summarized here. More information on this reduction package will be available in a forthcoming paper (Daigle et al. 2005).

3.1 Raw data integration and wavelength map creation

Files stored during an observation are made of the position of every photon that fell on the detector for a given FP position. The observed wavelength through a FP etalon is given by

$$p\lambda = 2ne\cos\theta,$$

where *p* is the interference order at λ_0 (Hα or 6562.78 Å for all observations presented in this paper), *n* the index of the medium, *e* the

distance between the plates of the FP and θ the incidence angle on the FP. For a given gap *e* and index *n*, every θ in a single channel is exposed to a different wavelength, which is to say that different pixels see different wavelengths. Thus, a phase calibration must be applied to transform raw interferograms into wavelength-sorted data cubes. This calibration is obtained by scanning a narrow Ne emission line. The bright line at 6598.95 Å has been chosen since it falls close to the redshifted Hα emission lines observed, limiting the phase shift in the dielectric layer of the FP. This calibration must be done in exactly the same conditions as the observations. It is thus convenient to acquire these calibration data just before starting an integration, when the telescope is already on the object. Since these calibrations are done with the camera in analogue mode (as compared to photon-counting mode), the overhead is very small (of the order of a minute). This allows one to perform a calibration at the beginning and at the end of an integration and to sum

Table 3. FaNTOmM characteristics on various telescopes.

Telescope name	D m[a]	F/D [b]	Pixel size (arcsec)[c]	FOV (arcmin)[d]	FOV$_{unvign}$ (arcmin)[e]
CFHT	3.6	2.96	0.48	5.83	3.91
ESO	3.6	3.44	0.42	5.01	5.01
OMM	1.6	2.00	1.61	19.43	19.43

[a] D: telescope diameter in metre.
[b] F/D: focal length over telescope diameter ratio calculated from the effective pixel size on the sky.
[c] Pixel size: pixel size after binning 2×2, the original GaAs system providing 1024×1024 pixel of 12.5 μm.
[d] FOV: diagonal field of view of the detector.
[e] FOV$_{unvign}$: unvignetted (usable) field of view.

them in order to average tiny variations of the FP etalon during the integration.

From these calibration data, a phase map is created. The phase map provides the shift that has to be applied in the spectral dimension to every pixel of the interferogram cube to bring all channels to the same wavelength. By applying this phase map to the interferogram data cube, the wavelength-sorted data cube is created. An uncertainty still remains on the zero point of the velocity scale since the observed wavelength is only known modulo the FSR of the interferometer

$$\text{FSR} \equiv \Delta\lambda = \frac{\lambda_0}{p}.$$

This uncertainty is removed by means of comparisons with long-slit spectroscopy or 21-cm H I data.

The computed wavelength of every slice of the resulting (calibrated) data cube is not absolute. When the observed wavelength is far from the calibration wavelength, the difference will increase. This is caused mainly by the semireflective, high Finesse coating of the FP etalon, which is hard to model. Absolute calibrations (in development), done at the same scanning wavelength, would be a way

Table 4. FP interferometer characteristics.

Interferometer	p	FSR	F	R
1	899	333.47	15.6–23.6	14294–21216
2	765	391.88	14.0–21.3	10710–16295
3	609	492.27	8.8–19.6	5259–14494

of getting rid of these differences. Absolute post-calibration using observed sky spectrum emission lines in the data cube, which must include compensation for the interference filter transmission curve, has been worked on but requires more testing to prove its accuracy. Nevertheless, *relative* wavelength measurements are accurate to a fraction of a channel (<0.05 Å) over the field. This leads to line of sight velocity (LOSV) measurement errors of less than 3 km s^{-1}.

Since the observational data are split in files representing a maximum of 15-s integration, it is possible to correct slight telescope guiding errors that could occur throughout the entire integration (typically 2–3 h). This correction must be made at the same time as the raw data integration. But, as a spatial translation in the interferogram domain will induce a wavelength shift in the spectral domain, the phase calibration must be applied at the same time as the raw integration. Results presented in this paper have undergone the phase calibration at the same time as the raw data integration in order to render guiding error corrections possible.

3.2 Sky emission removal

The sky emission in the neighbourhood of Hα at rest, caused by geocoronal OH molecules, is often stronger than the galaxy's diffuse Hα emission. It is thus highly important to properly remove this emission prior to the extraction of the radial velocity map. As opposed to the ADHOCW package, where the OH emission lines are removed by the subtraction of a single integrated profile taken from user-selected sky regions, the data presented in this paper have been processed differently. Due to inhomogeneities in the spatial and
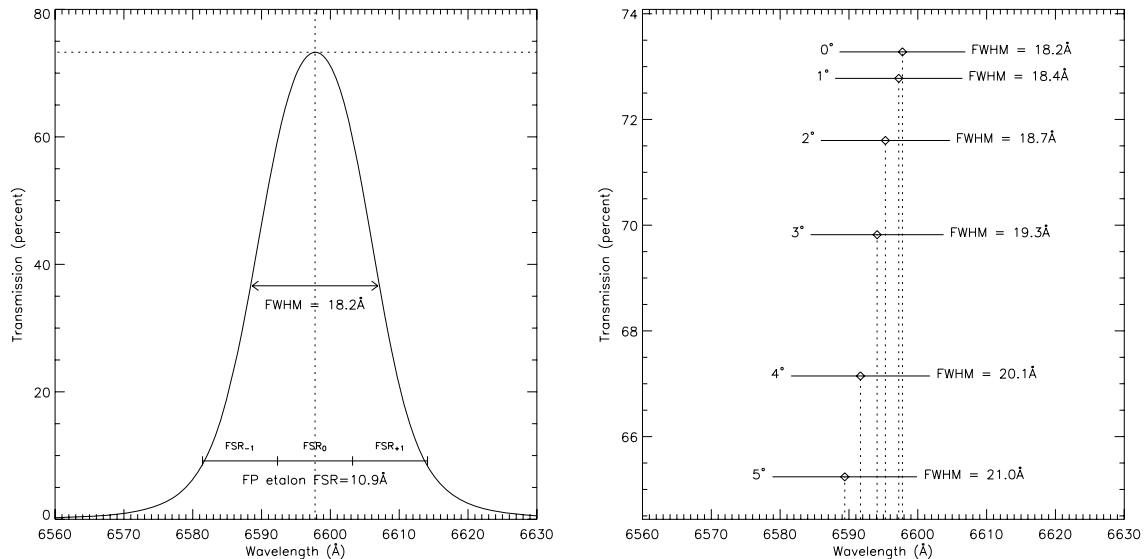
Figure 3. Left-hand panel shows a typical interference filter transmission curve (experimental data) at 20°C. As shown in the right-hand panel, filters may be tilted by a few degrees to blueshift the peak transmission wavelength by a couple of Å to allow it to be centred on the Hα emission of a galaxy, at the price of a broadened transmission curve and a decreased peak transmission. In the bottom of the left-hand panel is shown how FP interferometer and interference filters must be chosen to avoid having too many FSR to pass through the filter.

spectral responses of the interference filter, the subtraction of a single spectrum can lead to positive and negative residuals in the data cube, where not enough or too much of the spectrum were subtracted. To avoid having to deal with such issues and to improve the galaxies' signal coverage, a sky cube has been reconstructed by taking single pixel's spectra in the sky dominated regions and interpolating (or extrapolating) it in the galaxy's dominated spectra. This sky cube was then subtracted from the data cube. This proved to be a much better procedure. For best results, the surface covered by the sky dominated regions and the galaxy dominated regions should be in a ∼1:1 ratio.

3.3 Adaptive spatial binning and smoothing

In order to allow the LOSV of a galaxy's region to be properly determined, a minimum SNR is required. Cappellari & Copin (2003) used 2D Voronoi tessellations to create uniform SNR velocity maps of Sauron data. Starting from this work, an adaptive binning algorithm was developed for FP 3D data cubes. The main difference between the two algorithms is the way by which pixels are accreted into bins. Cappellari & Copin compute the SNR of a bin by means of

$$\text{SNR} = \frac{\sum_i \text{Signal}_i}{\sqrt{\sum_i \text{Noise}_i}},$$

where Signal_i and Noise_i are pre-computed signal and noise value of the spectra that will be binned; the SNR of the spectra presented in this paper has been recomputed each time a new spectrum was added to a bin. In short, each time a spectrum was added, it was summed with the other spectra of the bin, and a new SNR was recomputed by means of

$$\text{SNR} = \frac{N}{\sqrt{N + \sigma^2}},$$

where σ is the dispersion of the continuum of the spectrum and N the number of photons composing the emission line located above the continuum. Typically, a target SNR of 5 has been used. After the binning process, a Delaunay triangulation algorithm was used to smooth bins of each channel of the data cubes.

This smoothing method has been preferred to the fixed-sized kernel convolution (such as a 6 × 6 Gaussian). Adaptive spatial binning allows the spatial resolution to be kept in high SNR regions while still providing large signal coverage in low SNR regions.

3.4 Radial velocity map extraction

Radial velocity, monochromatic, continuum and dispersion maps are extracted with a single emission-line detection algorithm. This algorithm is based on barycentre computation. The central position of the emission line is computed with photons above the continuum that constitute the emission line. The radial velocity is then computed as

$$v_{\text{obs}} = \left[\frac{\left(\frac{\lambda_{\text{obs}}}{\lambda_0}\right)^2 - 1}{\left(\frac{\lambda_{\text{obs}}}{\lambda_0}\right)^2 + 1} + 1 \right] c + \text{corr},$$

where λ_{obs} is the emission line computed barycentre wavelength, λ_0 the rest wavelength (here, Hα), c the speed of light in vacuum and corr the heliocentric velocity correction computed for the time of the observation.

In the case where more than one velocity component is present in the spectrum, only the strongest emission line will be taken into

account. When two emission lines are spectrally close and have comparable amplitudes, they may be taken as a single one having a larger velocity dispersion. More details are available in Daigle et al. (2005).

3.5 Astrometry

Astrometric information was attached to the processed files by using the task KOORDS in the KARMA package (Gooch 1996). Right ascension, declination, pixel size and field rotation information are embedded in all files and permit their easy comparison with other survey images (DSS, 2MASS, *Spitzer*). To do so, original ADHOCW file types (ad2, ad3) were modified to allow these data to be stored. This is also an important step since the position angle (PA) of the major axis, whose determination is explained in the next section, is field orientation dependent. Moreover, the astrometric information is necessary to combine the kinematical data to the SINGS and ancillary multiwavelength surveys.

3.6 Kinematical parameters

The ROTCUR routine in the GIPSY package was used to find the kinematical parameters of the galaxies studied. ROTCUR works by fitting tilted-ring models to velocity information found in the velocity maps. V_{obs} is obtained using the following equation.

$$V_{\text{obs}} = V_{\text{sys}} + V_{\text{rot}}(R) \cos\theta \sin i + V_{\text{exp}}(R) \sin\theta \sin i,$$

where V_{sys} is the systemic velocity of the system studied, V_{rot} the rotation velocity, V_{exp} the expansion (non-circular) velocity, i the inclination of the ring, and R and θ the polar coordinates in the plane of the galaxy. The same procedure was used for all the galaxies of the sample. To allow for a good sampling frequency, the ring width used was always at least three times the pixel size.

The extraction of the kinematical parameters is done as follows. The photometric parameters of the galaxies [PA, inclination (i)] are taken from the RC3 catalogue as initial parameters. The photometric inclination is calculated as $I = \cos^{-1}(10^{-R_{25}})$. The rough rotational centre of the galaxies is taken by looking at the continuum maps extracted in Section 3.4 and taking the point where the continuum is the highest near the centre of the galaxy (usually obvious for spiral galaxies, trickier for irregular, low surface brightness and distorted ones). The starting point of the systemic velocity is the one used to select the interference filters, as explained in Section 2.2.

The initial photometric PA must be sometimes corrected (±180°) to properly represent the kinematical PA, that is, the angle from north-eastwards to the receding side of the galaxy. Also, GIPSY does not take into account the field rotation of the supplied radial velocity map. The starting PA is adjusted in order to reflect this.

First, ROTCUR is run to find the real kinematical centre of the galaxy and its systemic velocity by fixing both PA and i, and leaving the other parameters free. The analysis of the output of ROTCUR is made with IDL routines that permit the extraction of statistics on the free parameters, such as median, mean, error weighted mean, standard deviation and linear fit. If the output is too noisy, ROTCUR was run again, starting with another set of initial parameters, until the median of the absolute residual of the computed model was below 10 km s⁻¹. Then, having properly determined the kinematical centre and the systemic velocity, the real kinematical PA and inclination were set as free parameters, fixing all the others. Finally, having found the five kinematical parameters (x_c, y_c, V_{sys}, PA and

i), they were fixed and ROTCUR was run again to find V_{rot}. It was decided to use fixed values of PA and *i* across the whole galaxy as discs are rarely warped inside their optical part. Warps are mainly seen in discs for $R > R_{opt}$. However, the PA is observed to vary as function of radius for some galaxies (e.g. NGC 4579). The PA value is thus chosen in part of the disc where it reaches an almost constant value. The errors on the kinematical parameters found can thus be artificially lowered since the non-axisymmetric parts of the galaxies are discarded from the fit. For barred galaxies, this involved restricting the fit outside the bar. For non-barred galaxies, the outer parts were removed from the fit when the errors were larger than four times the mean error.

4 RESULTS

The kinematical parameters found by means of the method described in Section 3.6 are presented in Table 5.

In Appendix B, for each galaxy of the sample, the XDSS blue image, the *Spitzer* 3.6-μm image, the Hα monochromatic image, where the continuum has been suppressed, and the RV map are provided. A Position–Velocity (PV) diagram is given when it was possible to

Table 5. Photometic and kinematical parameters.

Galaxy name	Photometric[a]		Kinematical	
	PA(°)	Incl.(°)	PA(°)	Incl.(°)
NGC 628	25	24	26.4±2.4	21.5±4.5
NGC 925	102	56	105.0±1.0	50.0±1.5
NGC 2403	127	56	125.0±1.0	60.0±2.0
NGC 2798	160	68	−[b]	−[b]
NGC 2915	129	59	−[b]	−[b]
NGC 2976	323[c]	63	323.5±3.5	70.2±4
NGC 3049	25	49	−[b]	−[b]
NGC 3031	337[c]	58	332.9±1.2	62.4±1
UGC 5423	320[c]	49	320.5±5	58.8±6
NGC 3184	135	21	176.4±4[d]	16.7±1.1
NGC 3198	35	67	33.9±0.3	69.8±0.8
NGC 3521	343[c]	62	342.0±1.1	66.7±2
NGC 3621	339[c]	55	342.5±2.9	65.2±4
NGC 3938	151[c,e]	24	199.5±5[d]	7.7±3.2
NGC 4236	162	71	156.1±1.6	76.1±0.7
NGC 4321	30	32	27.0±1.0	31.7±0.7
NGC 4536	310[c]	65	300±2	68±3
NGC 4569	23	63	24.7±4.4	66.7±5
NGC 4579	95	37	89.5±4.5	45.7±7.3
NGC 4625	162[c,e]	29	126±5[d]	35.9±6
NGC 4725	35	45	30.3±1.6	50.8±2.1
NGC 5055	105	55	98.0±1.9	63±2
NGC 5194	163	52	169.0±4.2	47±5
NGC 5398	172	53	−[b]	−[b]
NGC 5713	190[c]	27	203±5.8	33±4.8
IC 4710	5	39	−[b]	−[b]
NGC 6946	250[c,e]	32	239.0±1.0	38.4±3.0
NGC 7331	171	69	165±1.2	78.1±2.7

[a]Photometric parameters taken from the RC3 catalogue.
[b]It is useless or impossible to determine the kinematical parameters for this galaxy due to either the lack of large-scale rotation or the interaction with another galaxy.
[c]A 180° rotation was applied to the photometric PA in order to be able to compare it with the kinematical PA.
[d]The photometric and kinematical PA do not agree even with a 180° rotation. This usually happens for face-on galaxies.
[e]This photometric parameter was not available in the RC3 data base and was taken from the 2MASS Large Galaxies Atlas.

extract the kinematical parameters from the radial velocity map. The red line superposed to the PV diagram is the velocity of the major axis of the galaxy's model reconstructed from its rotation curve. All images for a given galaxy have the same angular scale. Blue, IR and Hα monochromatic images have a logarithmic intensity scale. The colour scales of the radial velocity maps and the PV diagrams are linear.

Since the calibrations and the observations are most of the time done through different interference filters, the presented monochromatic maps could not be flux calibrated.

The rotation curves, extracted as explained in Section 3.6, are presented in Appendix C. The errors given for the velocity points are the difference between the approaching and the receding side of the galaxy or the formal error given by ROTCUR, whichever is the largest. We think that this is a better estimate than directly using the formal error of ROTCUR since this will take into account possible asymmetries between the two sides of the galaxies.

The rotation curves are available in electronic form at http://www.astro.umontreal.ca/fantomm/sings/rotation_curves.htm.

5 DISCUSSION

In this section, we discuss the advantages and limitations of Hα kinematic observations using integral field spectroscopy over other kinematical observational methods.

5.1 Better resolution of the inner rotation curve

Of course, the signal coverage of the Hα observations is less extended than for the H I observations, but it allows to resolve the rising part of the rotation curve with greater precision. Fig. 4 shows a 21-cm PV diagram of NGC 5055 taken from Wevers, van der Kruit & Allen (1986). From the 21-cm data alone, one can calculate that the maximum velocity gradient at the centre of the galaxy is of the order of ~ 45 km s^{-1} kpc^{-1}. The red line shows the rotation curve derived from the Hα data, which has a maximum gradient of ~ 300 km s^{-1} kpc^{-1}. This shows how the 21-cm data are affected by beam smearing. For H I, the beam full width half power (FWHP) is 49×73 arcsec^2 while the Hα resolution is 1.6×1.6 arcsec^2.

The rising part of the rotation curve is crucial in the determination of the dark-to-luminous mass ratio (Blais-Ouellette et al. 1999) and in the determination of the mass model parameters. For the sake of comparison, maximum achievable 21-cm beam width at the Very Large Array (VLA) in B configuration is ~ 4 arcsec usable only for the strongest emitting galaxies, while it is ~ 12.5 arcsec in C configuration, where sensitivity is high enough to observe the weak galaxies' signal. NGC 5055 harbours double emission lines in its centre, as noted by Blais-Ouellette et al. (2004). Resolving such details needs both the high spatial and spectral resolution of the integral field spectroscopy used throughout this study.

5.2 Better determination of the orientation parameters

One of the main advantage of the determination of galaxies' kinematics using integral field spectroscopy at Hα over long-slit spectroscopy is that there is no a priori knowledge needed on the galaxy apart from its systemic velocity (which is usually well known within a ± 50 km s^{-1} range for nearby galaxies, which is enough for accurate observations). In long-slit spectroscopic observations, the PA of the galaxy must be known as the slit must lie on the major axis.
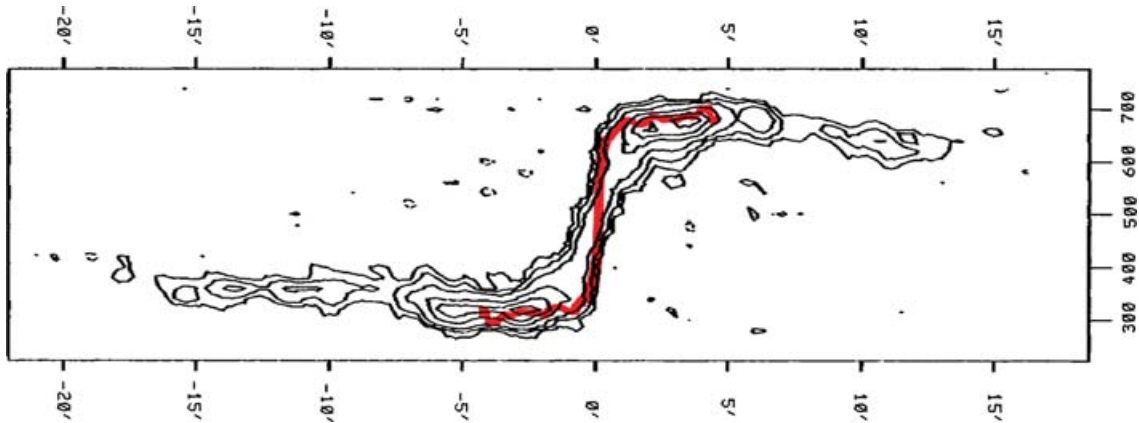
Figure 4. H I data of NGC 5055 taken from Wevers et al. (1986), and Hα rotation curve superposed on it (red line). This figure clearly shows the effect of beam smearing on H I data and the need for Hα data to resolve the kinematics at the centre of galaxies. In H I, the beam FWHP was 49×73 arcsec^2 while the Hα resolution is 1.6×1.6 arcsec^2.

The PA is thus usually determined by fitting ellipses to the optical isophotes. As Table 5 shows, there is sometimes a great discrepancy between published photometric and kinematical parameters.

The effect can be well illustrated with the nearly face-on ($i = 17°$) galaxy NGC 3184. The photometric PA of $135°$ is $41°$ off from the kinematical PA found. This PA error can lead to a substantial underestimate of the rotation velocities for highly inclined galaxies. Also, for some galaxies, the kinematical centre is not superposed on the photometric centre. This can also lead to large errors on the rotational velocities.

Fig. 5 shows the effect of using the photometric PA to observe this galaxy in long-slit spectroscopy. The resulting rotation curve is less steep in the centre of the galaxy, and the maximum rotational velocity is underestimated (rms error is 38.4 km s^{-1}), which affects the mass models used to determine the dark matter content. Using integral field spectroscopy, the kinematical PA is determined a posteriori and it does not affect the quality of the data gathered. The figure also presents the residuals of the velocity field models built from the rotation curves extracted. It clearly shows that had the kinematical data been gathered from long-slit observations using the photometric PA, the results would have been totally erroneous.

On the other hand, it should be considered that the difference between the photometric and kinematical PA may be partially due to the fact that the photometric PA would have been more accurately determined by using deep IR images (such as *Spitzer* images), which shows the old stellar population is less affected by structural patterns.

5.3 Observation of non-axisymmetric motions

Barred galaxies lead to a specific problem since errors on the determination of the PA of the disc can be induced by the bar. For instance, the galaxy NGC 3049 is totally dominated by a bar and its associated non-axisymmetric motions. By taking a look at the blue and IR images of Fig. B9, it could be thought, at first, that the PA is somewhere around $20°$. However, the isovelocity contours suggest that the PA is more like $60°$. This problem is caused by the lack of kinematical information outside the bar dominated region of the galaxy. In this case, H I data would be necessary to resolve the kinematics outside the bar, since the global kinematical parameters must be extracted from the axisymmetric portion of the galaxy.

This galaxy clearly demonstrates the advantage of 2D velocity fields over 1D long-slit data. 2D velocity fields allow to disentangle circular from radial motions while they would be confused in long-slit data. Integral field spectroscopy makes it possible to more thoroughly study non-circular motions in galaxies, such as in Hernandez et al. (2005a), where an in-depth study of barred galaxies is done.

5.4 Observation of highly inclined galaxies

It has been said that Hα could not resolve the kinematics for highly inclined galaxies since the gas cannot be considered optically thin at this wavelength (Goad & Roberts 1981). But, the case of NGC 4236, whose inclination is $76°$, shows that as long as the galaxy is not perfectly edge-on, the major axis of the galaxy is visible and the kinematics of the disc can be resolved. Fig. 6 shows how the Hα and H I kinematics agree. As opposed to the case of NGC 5055, we can compare the Hα kinematics to the H I kinematics since the inner part of the rotation curve is less shallow. However, since the signal coverage is less extended for Hα than it is for H I, the flat part of the rotation curve is missing from the Hα data. Also, as stated by Bosma et al. (1992), as spiral galaxies can be considered optically thin at least for the outer part of the visible disc ($R > 0.5R_{25}$), Hα observations can be used to resolve their kinematics.

6 CONCLUSION

The Hα kinematics of 28 galaxies of the SINGS survey were presented in this paper. The observations were made with FaNTOmM, an integral field FP spectrometer and a photon-counting camera. The raw data obtained at the telescope were processed through a new pipeline, an adaptive binning algorithm has been applied to achieve optimal SNR, and the radial velocity maps were finally extracted from the data cubes using a selective intensity weighted mean algorithm. Kinematical parameters were computed using a tilted-ring model, and most of them agreed within an acceptable error range with the photometric parameters, except for a few problematic galaxies. It has been shown that high spatial resolution data
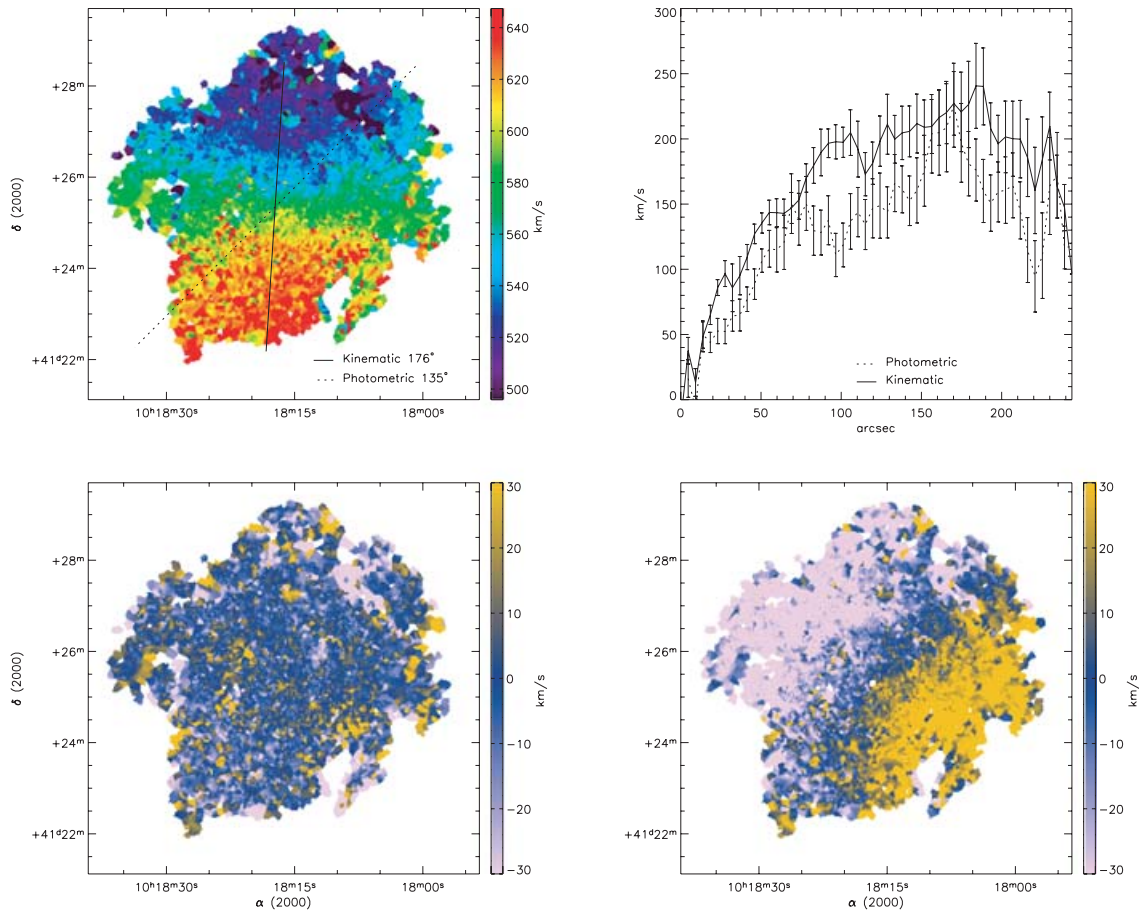
Figure 5. The difference between kinematical and photometric parameters for NGC 3184. Top left: Hα velocity field showing kinematical and photometric PA. Top right: rotation curves extracted from the velocity fields using kinematical and photometric parameters as if long-slit spectroscopy was used for the observations. The rms error of the photometric rotation curve is 38.4 km s^{-1}. There are nearly 30 per cent errors around 100 arcsec. Bottom left: residual map of a model built using the kinematical parameters. Bottom right: residual map of a model built using the photometric parameters.

Figure 6. NGC 4236 rotation curves obtained in Hα and H I. The H I data are taken from Huchtmeier (1975).

are essential for mapping the velocity gradient at the centres of galaxies. The advantages of integral field spectroscopy over long-slit spectroscopy were also presented.

The aim of this paper is to provide accurate optical kinematical data for the galaxies of the SINGS survey. These data will be used in a forthcoming paper to present rotation curves and mass models of the non-barred galaxies (Nicol et al. in preparation). The data of some of the barred galaxies of the SINGS sample that are also part of the

Big Hα survey of BARred galaxies (BHαBAR) survey were used to derive the bar pattern speeds using the Tremaine–Weinberg method (Tremaine & Weinberg 1984) in a paper presented by Hernandez et al. (2005b). These data might also be used to allow for some of the galactic star formation models to include kinematical data and thus try to determine what is the exact role of rotation in the star formation processes on a galactic scale.

The Hα kinematical data for all the observable SINGS galaxies will be made available to the community as soon as all the galaxies are observed.

ACKNOWLEDGMENTS

Innovation and the Ministère de l'Education du Québec. This project made use of the LEDA data base: http://leda.univ-lyon1.fr/. We also thank the anonymous referee for his valuable comments.

REFERENCES

Arsenault R., Roy J.-R., Boulesteix J., 1990, A&A, 234, 23
Begeman K. G., 1989, A&A, 223, 47
Blais-Ouellette S., Carignan C., Amram P., Côté S., 1999, AJ, 118, 2123
Blais-Ouellette S., Amram P., Carignan C., Swaters R., 2004, A&A, 420, 147
Boselli A., 2001, Ap&SS Supp., 277, 401
Bosma A., 1981, AJ, 86, 1791
Bosma A., Byun Y., Freeman K. C., Athanassoula E., 1992, ApJ, 400, L21
Broeils A. H., van Woerden H., 1994, A&AS, 107, 129
Bronkalla W., Notni P., Mutter A. A.-R., 1992, Astron. Nachr., 313, 1
Buta R., 1995, ApJS, 96, 39
Canzian B. J., 1990, PhD thesis, California Inst. of Tech., Pasadena
Canzian B., Allen R. J., 1997, ApJ, 479, 723
Cappellari M., Copin Y., 2003, MNRAS, 342, 345
Carignan C., Charbonneau P., Boulanger F., Viallefond F., 1990, A&A, 234, 43
Casertano S., van Gorkom J. H., 1991, AJ, 101, 1231
Cayatte V., van Gorkom J. H., Balkowski C., Kotanyi C., 1990, AJ, 100, 604
Cepa J., Beckman J. E., 1990, A&AS, 83, 211
Chemin L. et al., 2006, MNRAS, 366, 812
Conti P. S., 1991, ApJ, 377, 115
Corradi R. L. M., Boulesteix J., Bosma A., Amram P., Capaccioli M., 1991, A&A, 244, 27
Daigle, O., Carignan, C., Hernandez, O., Chemin L., Amram, P. 2006, MNRAS, submitted
del Burgo C., Laureijs R. J. Ábrahám P., Kiss C., 2003, MNRAS, 346, 403
Elmegreen B. G., Wilcots E., Pisano D. J., 1998, ApJ, 494, L37
Erwin P., 2004, A&A, 415, 941
Fraternali F., Oosterloo T., Sancisi R., van Moorsel G., 2001, ApJ, 562, L47
Gach J.-L. et al., 2002, PASP, 114, 1043
Garcia-Burillo S., Sempere M. J., Combes F., Neri R., 1998, A&A, 333, 864
Gil de Paz et al. 2005, ApJ, submitted
Goad J. W., Roberts M. S., 1981, ApJ, 250, 79
Gonzalez Delgado R. M., Perez E., 1996, MNRAS, 281, 1105
Gordon K. D. et al., 2004, ApJS, 154, 215
Helfer T. T., Thornley M. D., Regan M. W., Wong T., Sheth K., Vogel S. N., Blitz L., Bock D. C.-J., 2003, ApJS, 145, 259
Hernandez O., Gach J., Carignan C., Boulesteix J., 2003, SPIE, 4841, 1472
Hernandez O., Carignan C., Amram P., Chemin L., Daigle O., 2005a, MNRAS, 360, 1201
Hernandez O., Wozniak H., Carignan C., Amram P., Chemin L., Daigle O., 2005b, ApJ, 632, 253
Huchtmeier W. K., 1975, A&A, 45, 259
Kamphuis J., Briggs F., 1992, A&A, 253, 335
Kennicutt R. C., 1989, ApJ, 344, 685
Kennicutt R. C. et al., 2003, PASP, 115,928
Knapen J. H., Cepa J., Beckman J. E., Soledad del Rio M., Pedlar A., 1993, ApJ, 416, 563
Knapen J. H., Shlosman I., Heller C. H., Rand R. J., Beckman J. E., Rozas M., 2000, ApJ, 528, 219
Kuno N., Nakai N., 1997, PASJ, 49, 279
Marcelin M., Boulesteix J., Courtes G., 1982, A&A, 108, 134
Marcelin M., Petrosian A. R., Amram P., Boulesteix J., 1994, A&A, 282, 363
Marquez I., Moles M., 1996, A&AS, 120, 1
Meurer G. R., Carignan C., Beaulieu S. F., Freeman K. C., 1996, AJ, 111, 1551
Nishiyama K., Nakai N., Kuno N., 2001, PASJ, 53, 757
Nordgren T. E., Helou G., Chengalur J. N., Terzian Y., Khachikian E., 1995, ApJS, 99, 461
Pellet A., Simien F., 1982, A&A, 106, 214
Pisano D. J., Wilcots E. M., Elmegreen B. G., 1998, AJ, 115, 975
Pogge R. W., 1989, ApJS, 71, 433
Rand R. J., 1995, AJ, 109, 2444
Regan M. W. et al., 2004, ApJS, 154, 204
Rosenberg J. L., Schneider S. E., 2003, ApJ, 585, 256
Rots A. H., Crane P. C., Bosma A., Athanassoula E., van der Hulst J. M., 1990, AJ, 100, 387
Sakamoto K., Okumura S., Minezaki T., Kobayashi Y., Wada K., 1995, AJ, 110, 2075
Sandage A., 1986, ARA&A, 24, 421
Schaap W. E., Sancisi R., Swaters R. A., 2000, A&A, 356, L49
Schoenmakers R. H. M., Franx M., de Zeeuw P. T., 1997, MNRAS, 292, 349
Shostak G. S., 1973, A&A, 24, 411
Sofue Y., Tomita A., Tutui Y., Honma M., Takeda Y., 1998, PASJ, 50, 427
Sofue Y., Koda J., Nakanishi H., Onodera S., Kohno K., Tomita A., Okumura S. K., 2003, PASJ, 55, 17
Stil J. M., Israel F. P., 2002, A&A, 389, 42
Tilanus R. P. J., Allen R. J., 1991, A&A, 244, 8
Tosaki T., Shioya Y., 1997, ApJ, 484, 664
Tremaine S., Weinberg M. D., 1984, ApJ, 282, L5
Tschöke D., Bomans D. J., Hensler G., Junkes N., 2001, A&A, 380, 40
van der Kruit P. C., Shostak G. S., 1982, A&A, 105, 351
van Moorsel G. A., 1983, A&AS, 54, 19
Vogt N. P., Haynes M. P., Herter T., Giovanelli R., 2004, AJ, 127, 3273
Vollmer B., Balkowski C., Cayatte V., van Driel W., Huchtmeier W., 2004, A&A, 419, 35
Wevers B. M. H. R., van der Kruit P. C., Allen R. J., 1986, A&AS, 66, 505
Willner S. P. et al., 2004, ApJS, 154, 222
Young J. S. et al., 1995, ApJS, 98, 219

APPENDIX A: DESCRIPTION OF THE INDIVIDUAL GALAXIES

A brief description of the structures observed in the Hα velocity fields, monochromatic images and PV diagrams of the SINGS sample is given in this appendix. The galaxies NGC 0925, 2403, 3198, 4236, 4321 and 6964 are part of the *B*HαBAR survey and are extensively described in Hernandez et al. (2005a). The galaxies NGC 4321, 4536, 4569 and 4579 are part of the sample of 30 Virgo cluster galaxies and will be studied in Chemin et al. (2005).

NGC 628 (M74): the H I PA of this face-on galaxy varies greatly with distance from the centre, as observed by Kamphuis & Briggs (1992). In the visible, this phenomenon is seen in the outer rings of the Hα RV map. Some H II regions with velocities that are perpendicular to the plane of the galaxy are also visible. The H I PA determined by Kamphuis & Briggs (1992) agrees with the kinematical one (Table 5), but the inclination differs greatly (6.5° for H I and 21.5° for Hα). This may be due to the fact that ROTCUR has problems dealing with galaxies whose inclination is <40° (Begeman 1989; Chemin et al. 2005). For the rotation curve presented in Fig. C1, the H I inclination was adopted. This galaxy has also been observed in CO by Nishiyama, Nakai & Kuno (2001).

NGC 925: this late-type SBcd galaxy has a bright optical and Hα bar and two bright patchy spiral arms beginning at the ends of the bar. Many H II regions lie along the bar. The photometrical and kinematical data agree. The PV diagram shows non-axisymmetric motions near the centre. It is well studied in H I (Elmegreen, Wilcots & Pisano 1998; Pisano, Wilcots & Elmegreen 1998), in CO (Helfer et al. 2003) and in Hα (Marcelin, Boulesteix & Courtes 1982). It shows strong streaming motions.

NGC 2403: this SABc galaxy shows amorphous spiral features. The Hα velocity maps and the PV diagram show an almost rigid structure near the centre of the galaxy. Bright H II regions can be

seen in the Hα monochromatic image. It is not clear whether this galaxy is barred or not. According to Schoenmakers, Franx & de Zeeuw (1997), their Fourier harmonic analysis of the H I velocity field shows that non-circular motions are not important in this galaxy. Moreover, Schaap, Sancisi & Swaters (2000) stress that the thin hydrogen disc of NGC 2403 is surrounded by a vertically extended layer of H I that rotates slower than the disc. A complete modelling of the galaxy will provide more details on its structures. Fraternali et al. (2001) suggest that this anomalous H I component may be similar to a class of high-velocity clouds observed in the Milky Way. In CO data, no molecular gas is detected (Helfer et al. 2003).

NGC 2798: this galaxy is interacting with its close companion, NGC 2799, on the east. Marquez & Moles (1996) observed a difference of $125 \, \mathrm{km \, s^{-1}}$ in the velocity of the H I and H II components of NGC 2799. Due to this interaction, it was useless to determine the kinematical parameters of this galaxy (Table 5).

NGC 2915: the radial velocity map of this galaxy shows a highly distorted optical disc. This renders the determination of the kinematical parameters of the galaxy impossible. Two bright H II regions are visible towards the centre of the galaxy. Meurer et al. (1996) obtained the H I kinematics of this blue compact dwarf galaxy. They observed that the optical disc of the galaxy corresponds to the central H I bar. They think that the dark matter halo dominates at nearly all radii.

NGC 2976: this peculiar dwarf late-type galaxy has a nearly linear rotation curve. There is no spiral arm visible. Two strong H II regions are located on each side of the galaxy. Stil & Israel (2002) observed that in H I the rotation curve seems to flatten near the edge of the H I disc. According to Bronkalla, Notni & Mutter (1992), the outer parts of NGC 2976 have been undisturbed for a long time and are very old (5 Gy, probably up to 15 Gy).

NGC 3031 (M81): the great M81 spiral galaxy has few Hα emission in its centre, given its somewhat early type (Sab). The velocity information for radii up to ∼4 arcmin is thus difficult to extract. Farther away from the centre, the rotation curve is very flat and does not show any decrease near the edge of the optical disc. Long-slit observations performed by Pellet & Simien (1982) show the same flattening. The bright core, as seen in IR, contrasts greatly with its dim Hα counterpart. Detailed investigation of the UV, Hα and IR SFR indicators based on *Spitzer* and SINGS ancillary data has been done by Gordon et al. (2004) and suggests that the central dust is heated by stars in the bulge rather than star formation. The morphological analysis of the IR data has been done by Willner et al. (2004), and shows evolved stars organized in bulge and disc components, a dusty ISM showing star-forming regions and a clumpy profile. Still, according to Willner et al., the flux density of the point-like nucleus seems to have decreased by a factor of 3 in the past 4 yr.

NGC 3049: this Makarian galaxy harbours a 'double nucleus', as stated by Nordgren et al. (1995). This feature, invisible in IR, is easily seen in Hα and it does not seem to affect the galaxy's kinematics. The 'second nucleus' is most probably just a strong starburst H II region. Still, according to Nordgen, this galaxy does not show any trace of merging. The galaxy is totally dominated by a bar, and the signal is too weak outside the bar to resolve the kinematics, rendering the extraction of kinematical parameters impossible.

UGC 5423 (M81 dwarf B): we present the first available kinematical data for this dwarf galaxy. Rotation is weak.

NGC 3184: CO kinematics have been obtained by Nishiyama et al. (2001) for this nearly face-on galaxy. Hα data show a pretty flat rotation curve that nearly reaches a flat part within the optical disc.

NGC 3198: this SB(rs)c galaxy has been extensively studied in H I (Bosma 1981; Begeman 1989), FP Hα (Corradi et al. 1991; Blais-Ouellette et al. 1999) and Hα and [N II] long-slit spectroscopy (Sofue et al. 1998; Vogt et al. 2004). According to the PV diagram, non-circular motions near the centre can be seen. A strong velocity gradient is also seen perpendicular to the bar major axis.

NGC 3521: the declining H I rotation curve of this galaxy allowed Casertano & van Gorkom (1991) to call for the end of the 'disc–halo conspiracy'. Though not visible in Hα, the rotation curve starts to decline within a radius of 22 kpc, and the Hα data stop at 13 kpc.

NGC 3621: many strong H II regions are visible in this galaxy at all galactic radii. The Hα data do not seem to reach the flat part of the rotation curve. This galaxy has been observed by using three fields of the ESO/La Silla 3.6-m telescope. More kinematical data could be gathered by observing further north and south of the galaxy.

NGC 3938: the nearly face-on orientation of this galaxy allowed van der Kruit & Shostak (1982) to study it in H I to search for extra-planar velocity components. An in-depth study of the Hα velocity map is required in order to corroborate this.

NGC 4236: this late-type SBdm galaxy is seen nearly edge-on. Its kinematical inclination is $76°$. The Hα image shows that the H II regions are distributed along the bar, with two bright regions near the end of the bar. These features are also seen in H I (Shostak 1973). An extensive region of solid-body rotation coincides with the bar.

NGC 4321 (M100): this grand-design spiral galaxy is located in the Virgo cluster. It has been frequently mapped in the Hα emission line using high-resolution FP interferometry (Arsenault, Roy & Boulesteix 1990; Cepa & Beckman 1990; Canzian & Allen 1997; Knapen et al. 2000), in the molecular CO emission line (Canzian 1990; Rand 1995; Sakamoto et al. 1995; Garcia-Burillo et al. 1998; Helfer et al. 2003) and in the 21-cm H I emission line (Cayatte et al. 1990; Knapen et al. 1993). The H I disc is almost totally confined within the optical one but with a slight lopsidedness towards the south-west (Knapen et al. 1993). The H I, CO and Hα velocity fields show kinematical disturbances such as streaming motions along the spiral arms and a central S-shape distortion of the iso-velocity contours along the bar axis. The circum-nuclear region shows the presence of an enhanced star formation region as a four-armed Hα ring-like structure and a CO & Hα spiral-like structure. Much more details can be found in Hernandez et al. (2005a) and in Chemin et al. (2005).

NGC 4536: streaming motions along the spiral arms and a Z shape of the velocities in the central parts are observed in this barred galaxy. As in the CO data (Sofue et al. 2003), a steep velocity gradient is observed in the Hα data.

NGC 4625: this galaxy has a close companion, lying 8 arcmin away, which is only 22-kpc distant. The galaxy has a very weak rotation and harbours a lot of double profile emission lines, a sign of non-circular activity. This explains the large errors on the kinematical parameters found and the 'boiling' aspect of the Hα velocity field extracted. van Moorsel (1983) studied it in H I and found a neutral hydrogen disc having a diameter of 5 arcmin, which is approximately five times larger than the observed Hα disc. GALEX images of this galaxy show a very extended UV disc, extending at least 2–3 times the radius of the main star-forming disc (Gil de Paz et al. 2005).

NGC 4569 (M90): this galaxy is located in the Virgo cluster. An off-plane structure to the west of the disc of NGC 4569 has been seen through deep Hα imaging (Tschöke et al. 2001) and

in H I data (Vollmer et al. 2004). It is observed here as a string of H II regions whose kinematics follow the rotation of the disc, although it is slightly more redshifted than inside the disc at equal azimuth angles (Chemin et al. 2005).

NGC 4579 (M58): in addition to the main large-scale spiral arms, this Virgo galaxy exhibits a nuclear spiral structure [the so-called 'loop' in Pogge (1989) and Gonzalez Delgado & Perez (1996)] within which is detected a gradient of up to $\sim$500 km s^{-1}. The FP velocity field shows that the kinematical PA of this nuclear spiral differs by $\sim$90° from that of the main spiral arms. The kinematical parameters of this galaxy shown in Table 5 are calculated for the grand-design spiral structure (i.e. outside of the nuclear spiral structure) (see Fig. B19). The PA of the nuclear structure is $\simeq$174° $\pm$ 11 (Chemin et al. 2005).

NGC 4725: this barred ringed Sab lenticular galaxy is catalogued as a double barred galaxy by Erwin (2004) and H I rich by Rosenberg & Schneider (2003). No kinematical data are available for this galaxy. The kinematics in the centre of the galaxy are hard to resolve given its early type.

NGC 5055 (M63): this galaxy shows several arm patterns that are well visible in Hα. It harbours a very strong velocity gradient in its centre and a flat rotation curve. No bar structure is visible. It has been studied in H I by Bosma (1981) and in CO by Nishiyama et al. (2001). This galaxy has also been studied in Hα by Blais-Ouellette et al. (2004), which showed two velocity components in its central region. The Hα images presented in this paper have weaker response on the receding side of the galaxy than on the approaching side due to the wide span in the galaxy's velocities which made the receding emission fall on the wing of the interference filter.

NGC 5194 (M51a): two emission lines are visible in the very centre of the galaxy and may account for the 'dip' in the rotation curve shown in the PV diagram. The strong H II regions discriminate the great spiral structure from the rest of the galaxy. A flow of H II regions is seen extending towards its companion. This galaxy has been studied in H I by Rots et al. (1990), in both H I and Hα (scanning FP) by Tilanus & Allen 1991) and more recently in CO by Kuno & Nakai (1997). NGC 5195, the galaxy's compan-

ion, has been observed in Hα through this study, but it is impossible to get kinematical information as it is an early-type galaxy (SB0p).

NGC 5398: this study provides the first kinematical data for this galaxy. Its peculiar radial velocity map makes it impossible to extract kinematical parameters. It has been classified as ringed galaxy by Buta (1995) and Wolf–Rayet galaxy by Conti (1991).

NGC 5713: many strong H II regions are visible in this galaxy and produce an oddly looking radial velocity map. There were no kinematical data available for this galaxy prior to publishing this paper.

IC 4710: this galaxy has plenty of H II regions but does not seem to harbour large-scale rotation.

NGC 6946: according to H I studies (Carignan et al. 1990), the H I distribution is not symmetric but is more extended to the northeastern side. This feature is also seen in the Hα emission map. The overall Hα velocity map is regular but shows some non-circular motions near the centre, confirmed by the PV diagram. It has been recently observed in FP by Blais-Ouellette et al. (2004) leading to the same conclusions. Once again, the wide field of FaNTOmM and its high sensitivity are clearly an advantage to obtain better Hα velocity fields. CO data have been gathered by Young et al. (1995).

NGC 7331: the receding part of the galaxy is invisible in the RV maps presented in this paper. It was first thought that this part of the galaxy was out of the interference filter, but this feature has also been observed by Marcelin et al. (1994). An a posteriori scan of the interference filter used showed that the galaxy should have been well centred in the filter. Deep Hα images taken by Regan et al. (2004) at the KPNO 2.1-m telescope show the same asymmetric emission pattern. However, Regan et al. (2004) also made Paα observations and did not observe that asymmetry. A theory to explain this is that a ring of dust located south of the centre of the galaxy is blocking the Hα emission from reaching us whilst letting the Paα through. This galaxy has been called 'Post-starburst' by Tosaki & Shioya (1997) who studied its kinematics in CO. CO data have also been gathered by Nishiyama et al. (2001).
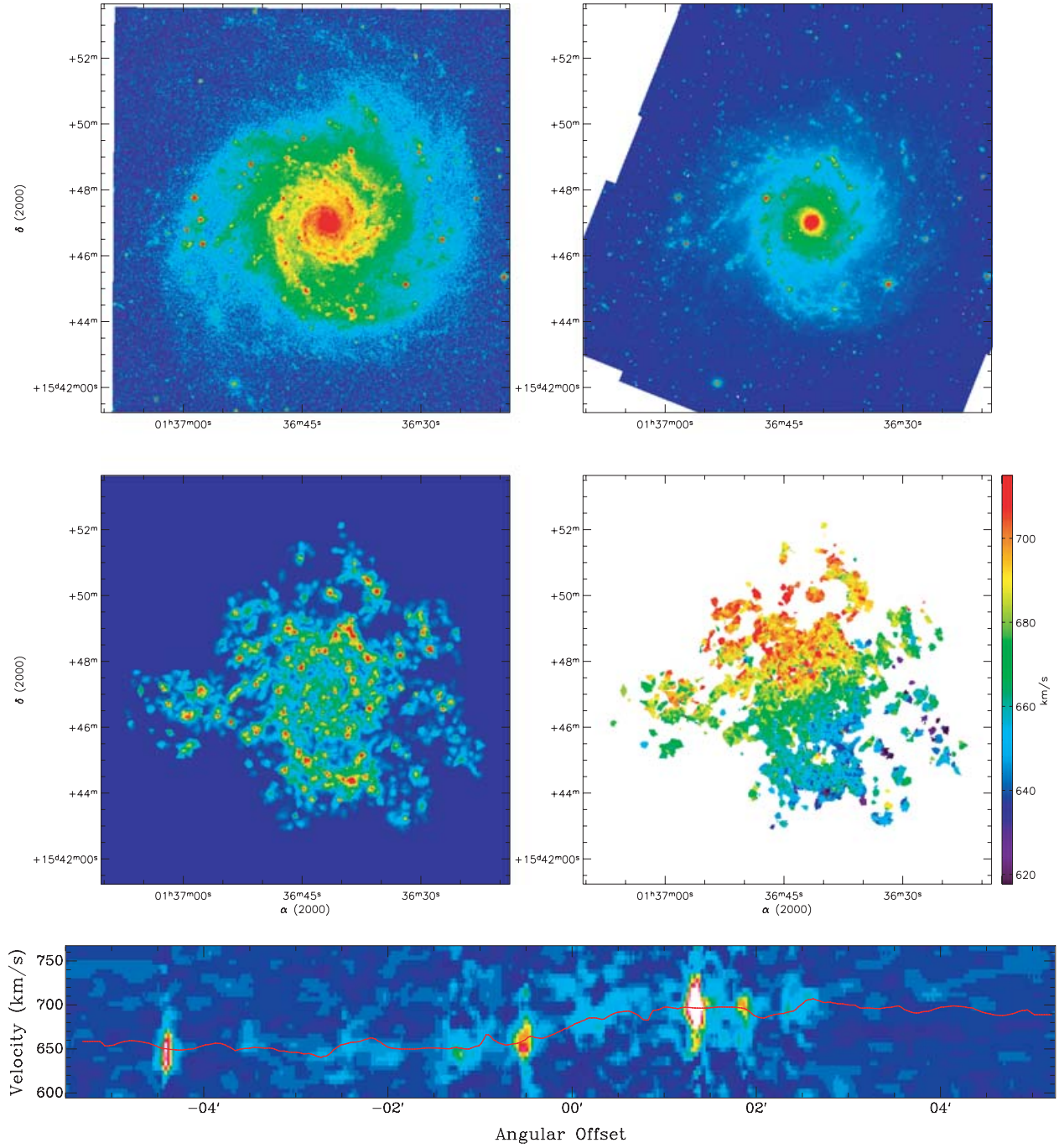
APPENDIX B: OBSERVATIONAL DATA

NGC 628

Figure B1. NGC 628. Top left: XDSS Blue Band image. Top right: *Spitzer* IRAC 3.6-µm image. Middle left: Hα monochromatic image. Middle right: Hα velocity field. Bottom: PV diagram.
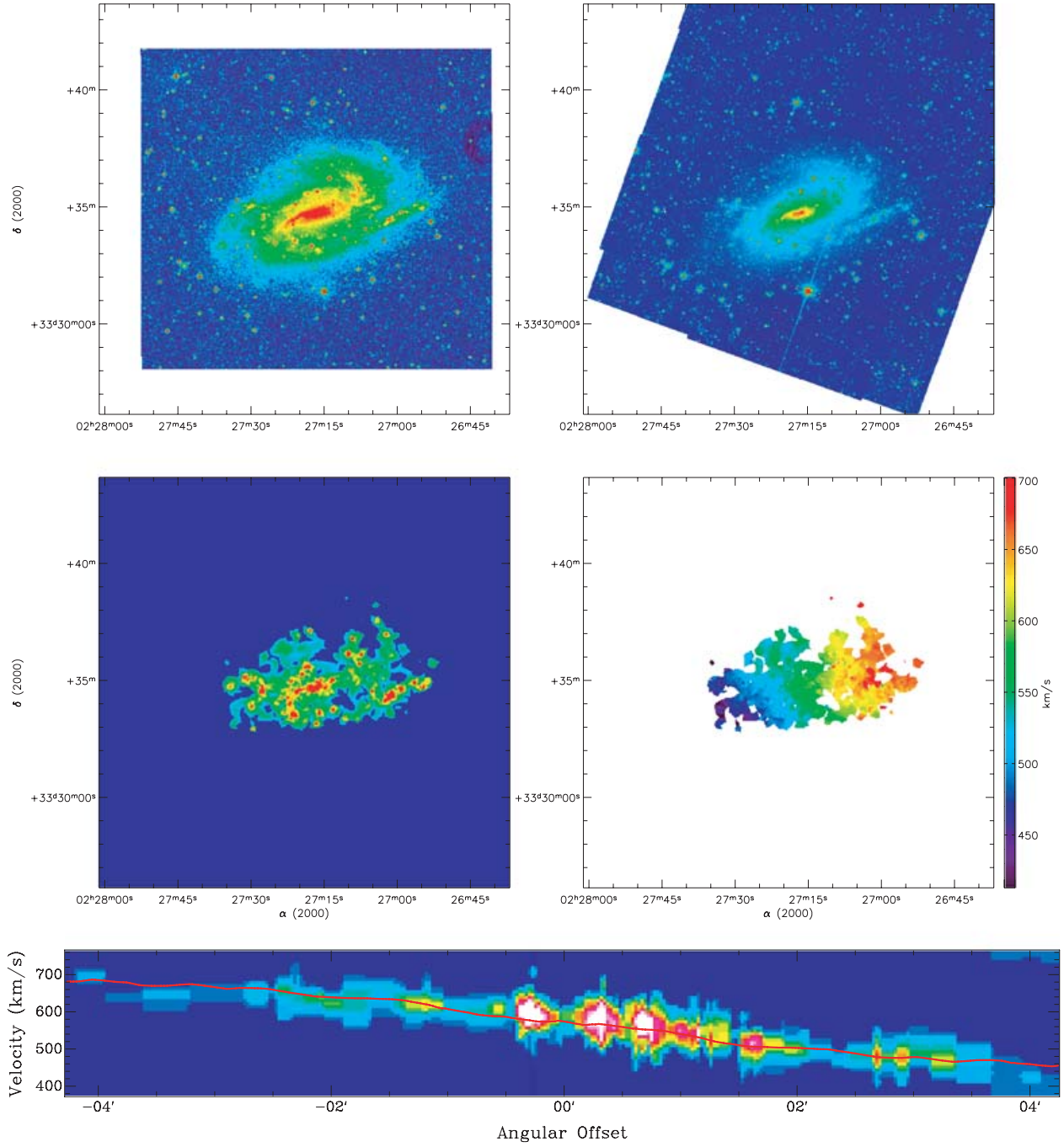
NGC 925

Figure B2. NGC 925. Top left: XDSS Blue Band image. Top right: *Spitzer* IRAC 3.6-μm image. Middle left: Hα monochromatic image. Middle right: Hα velocity field. Bottom: PV diagram.
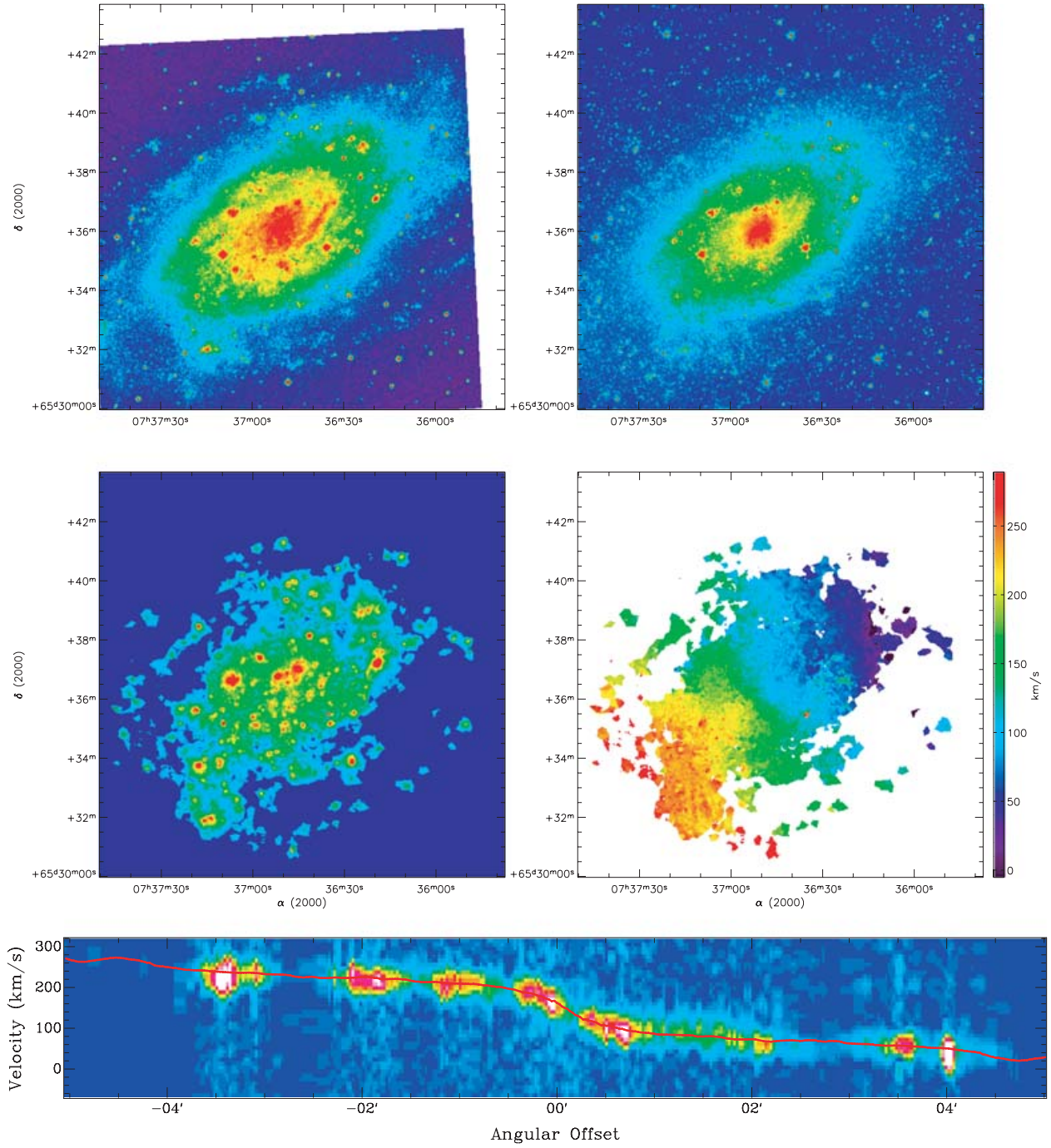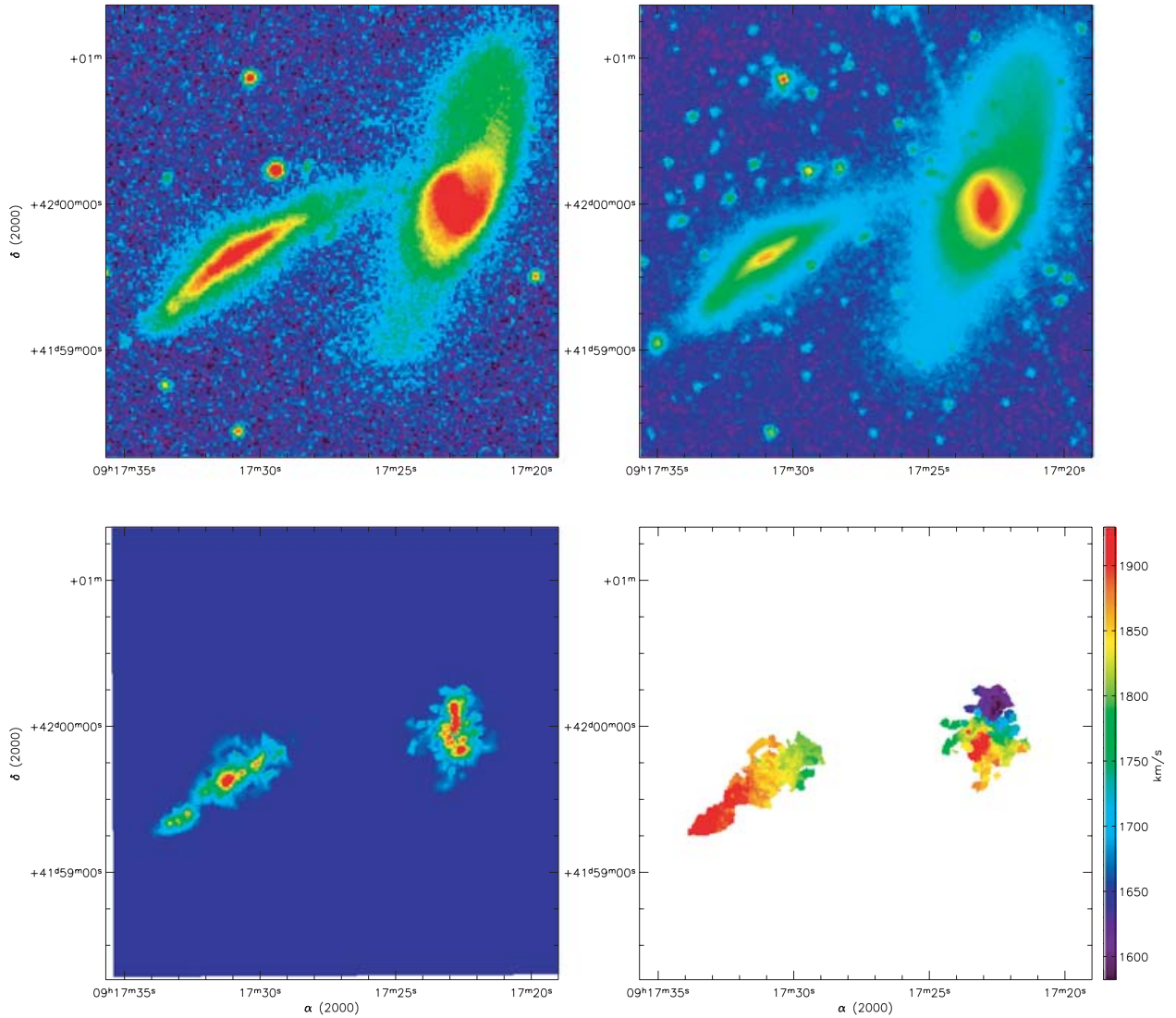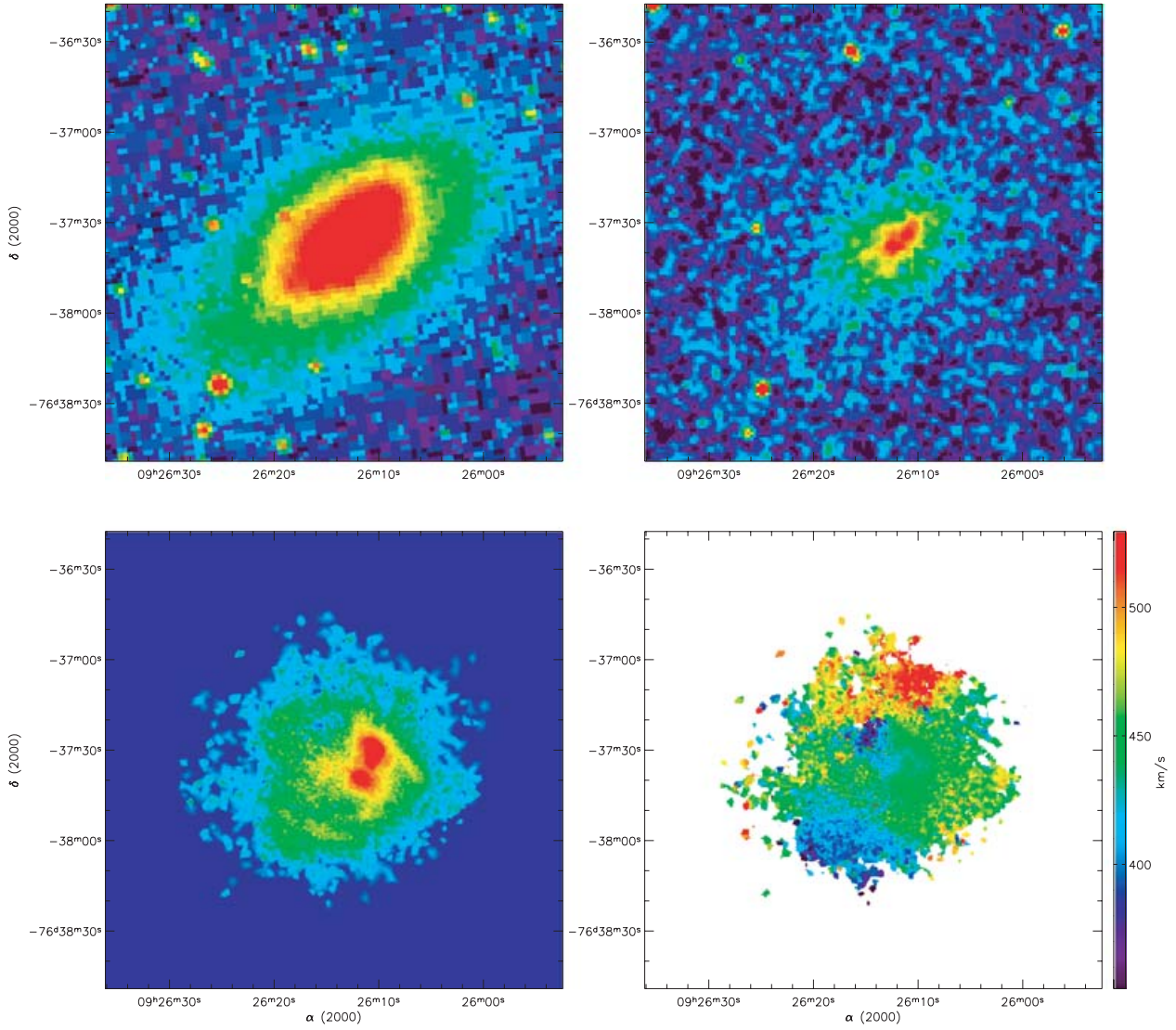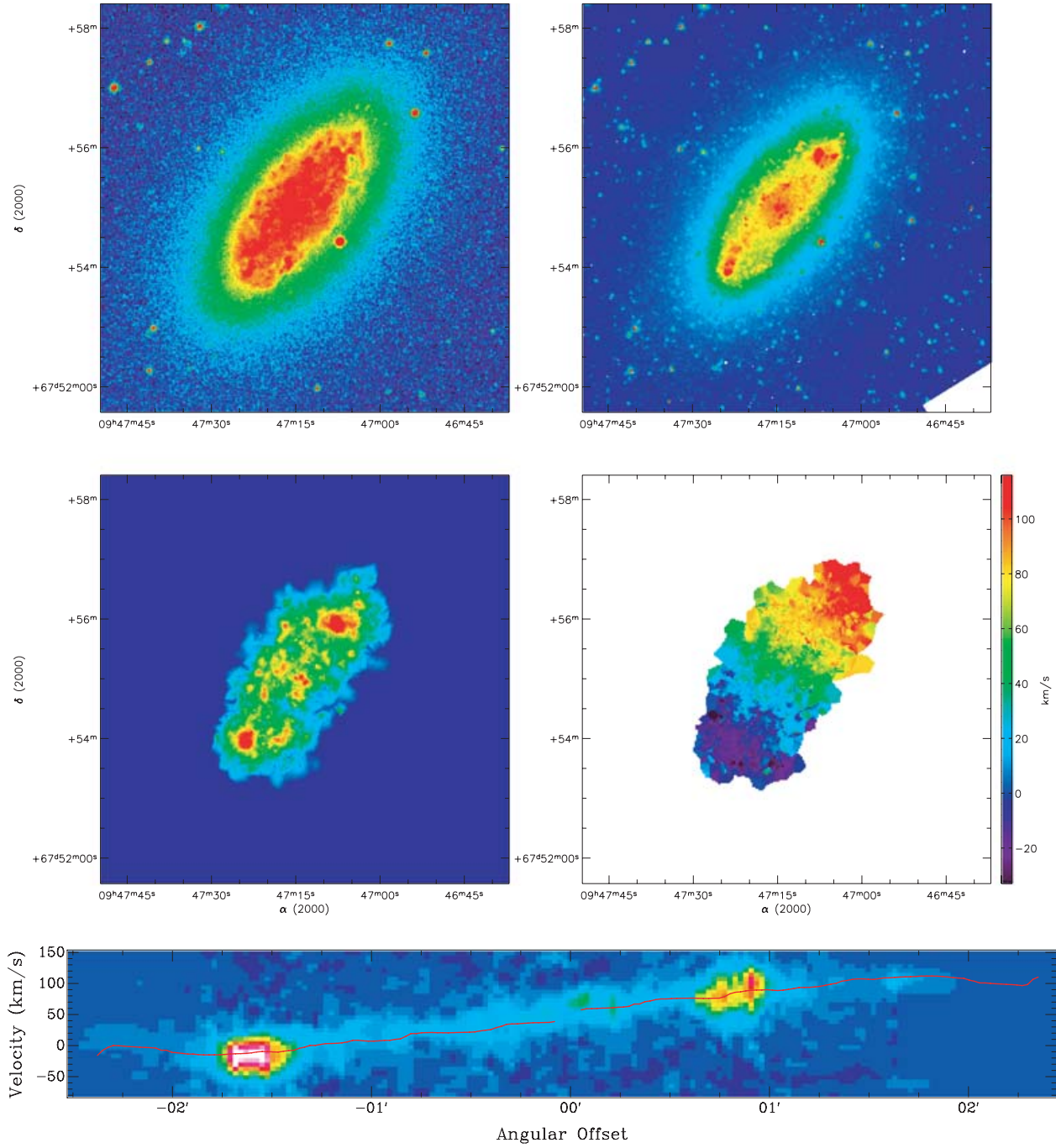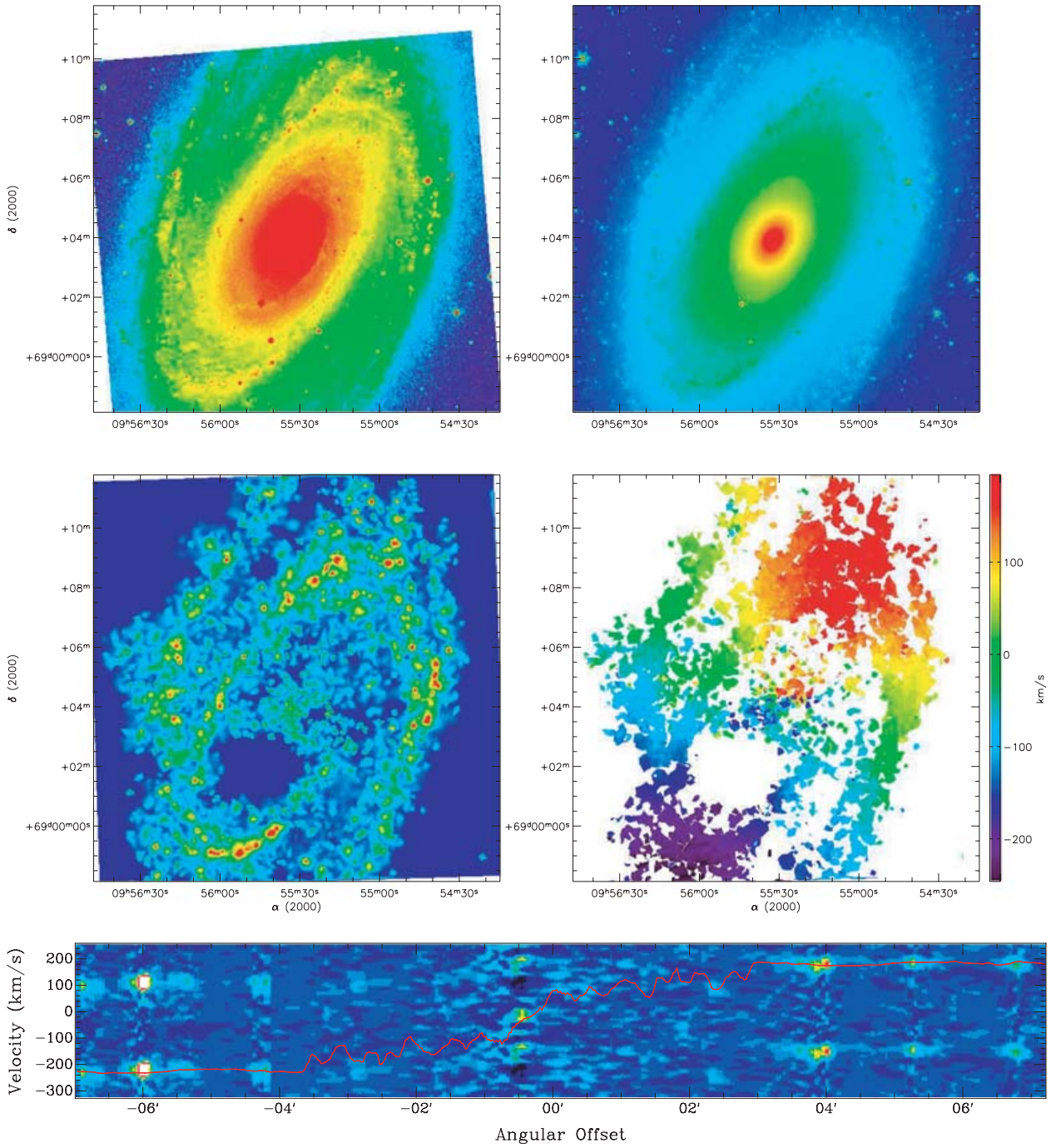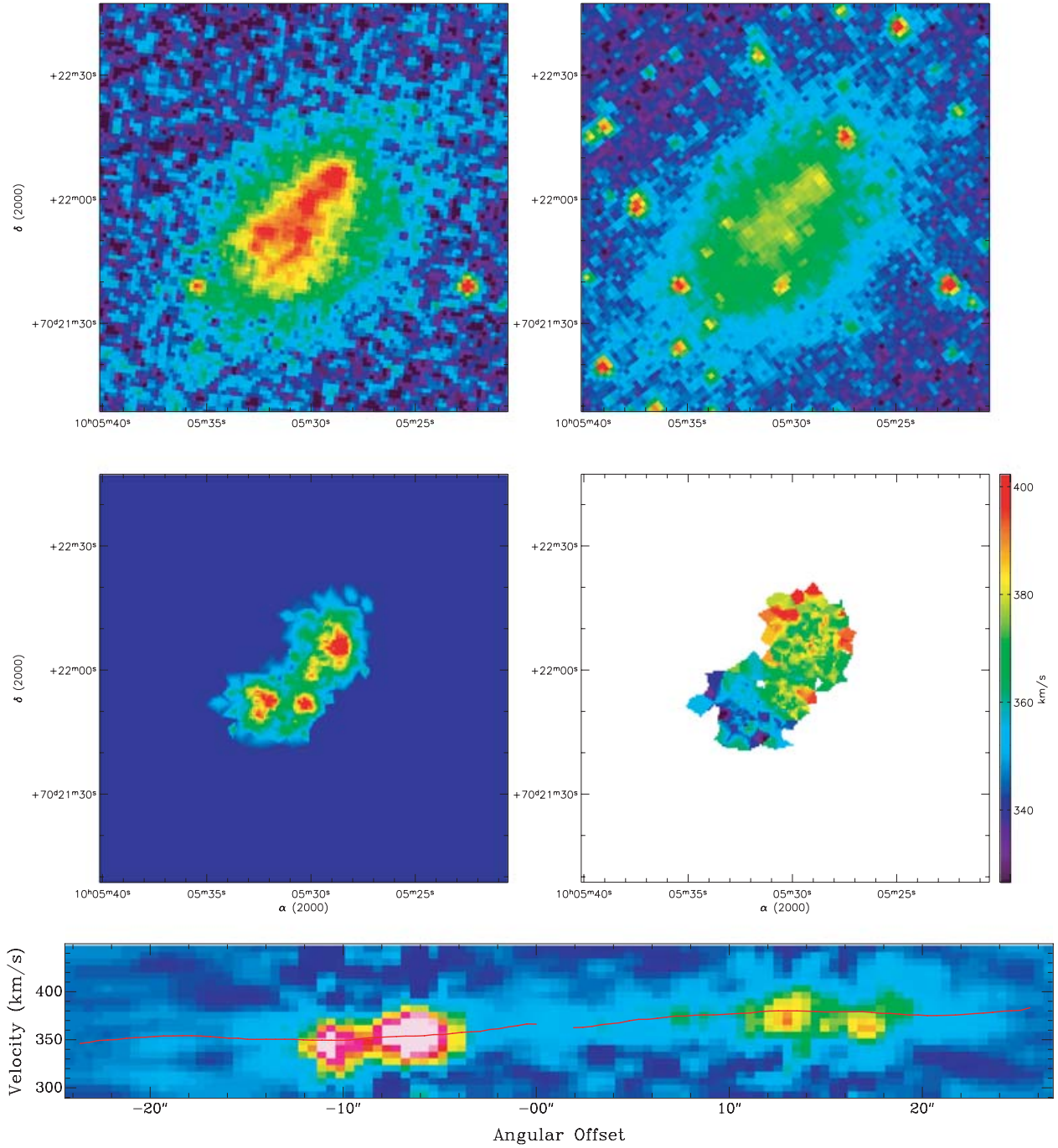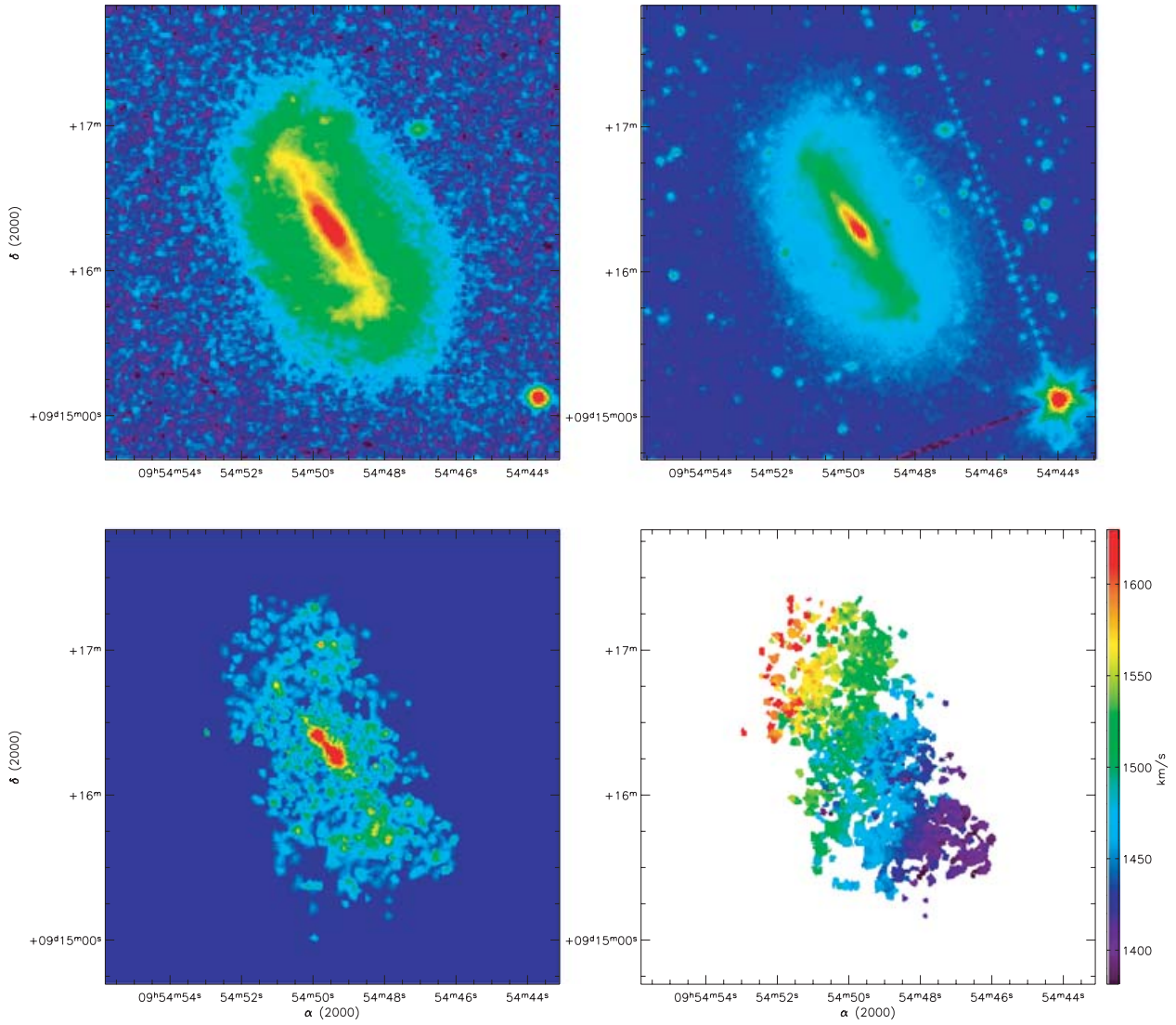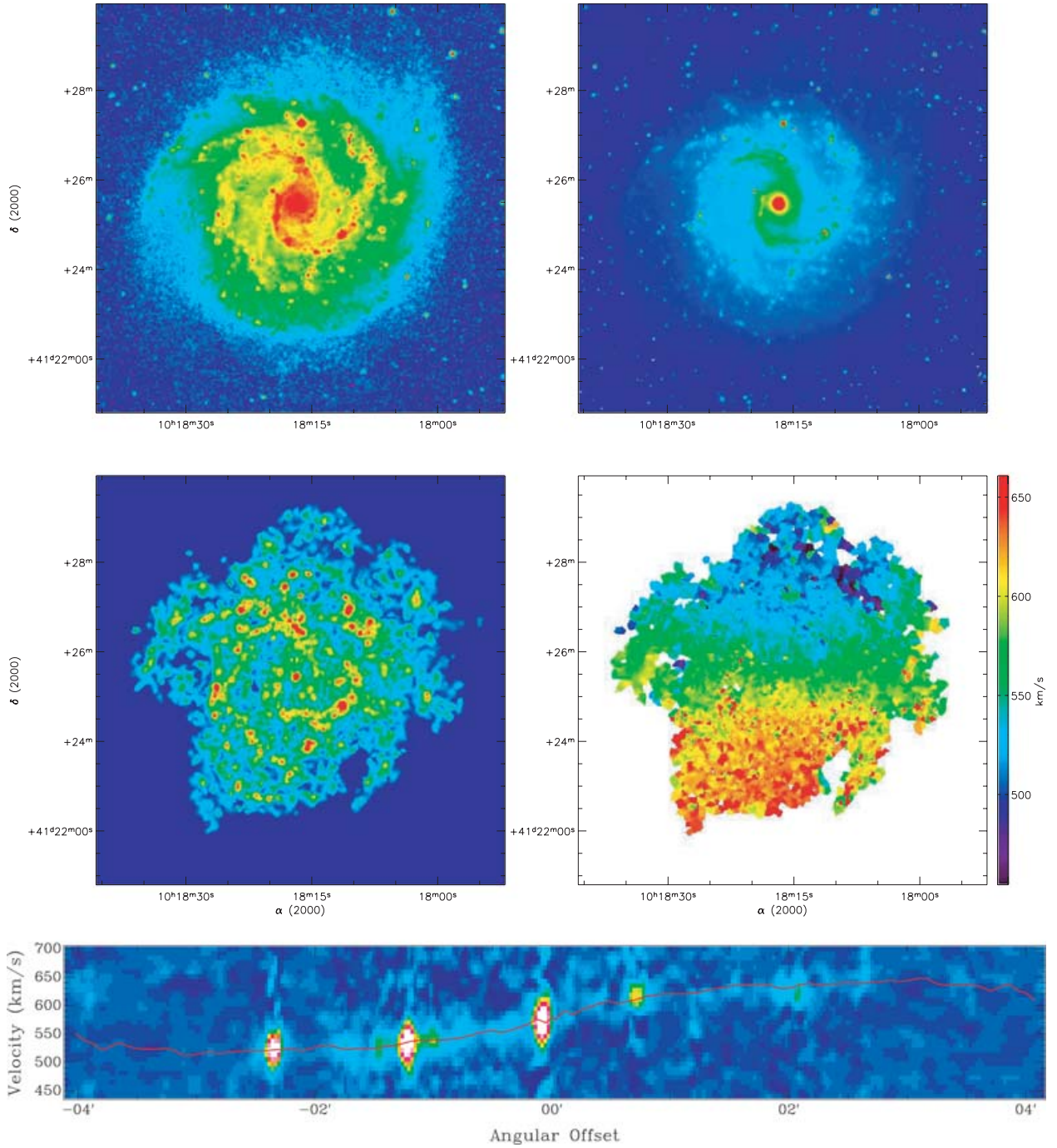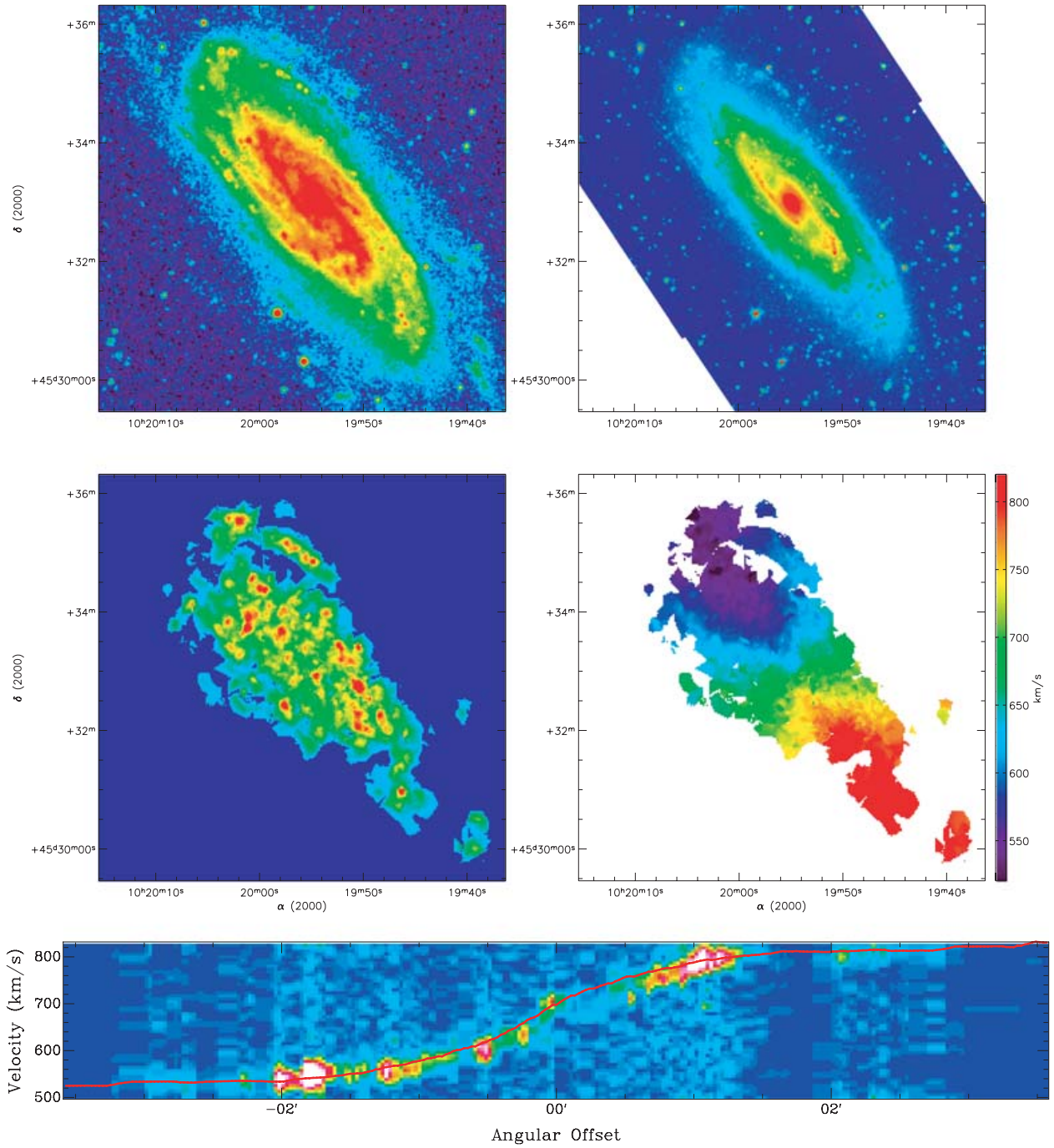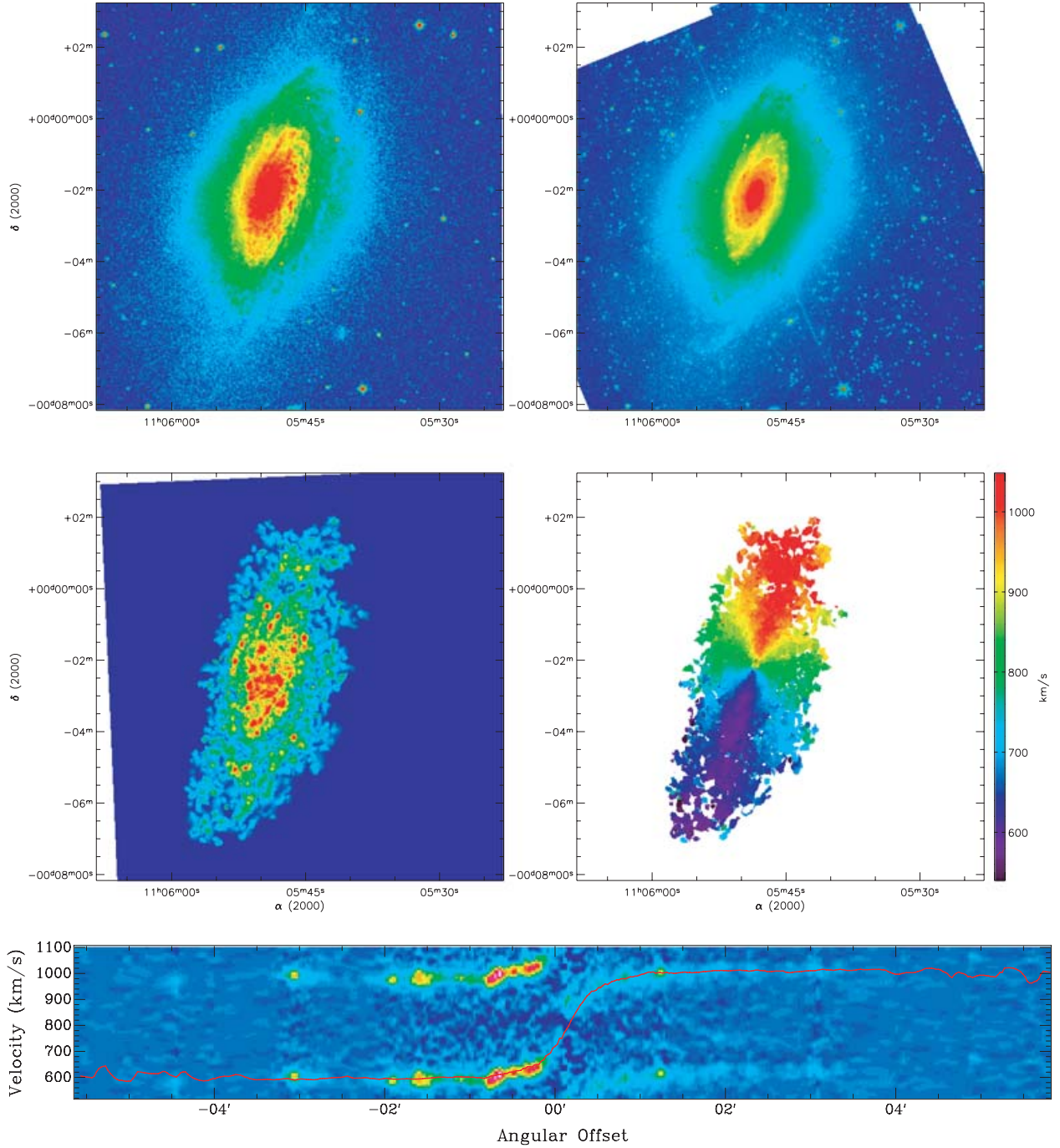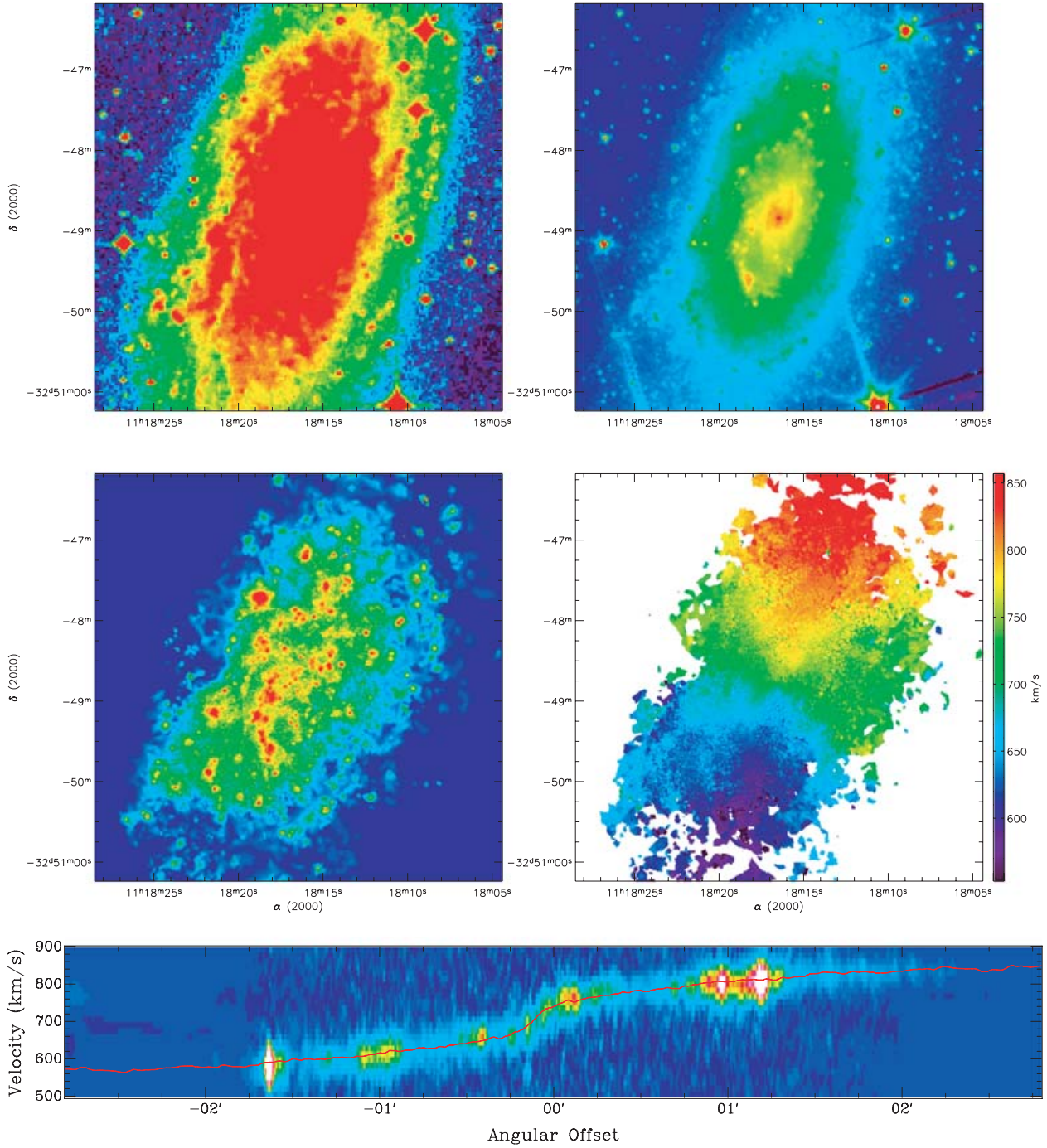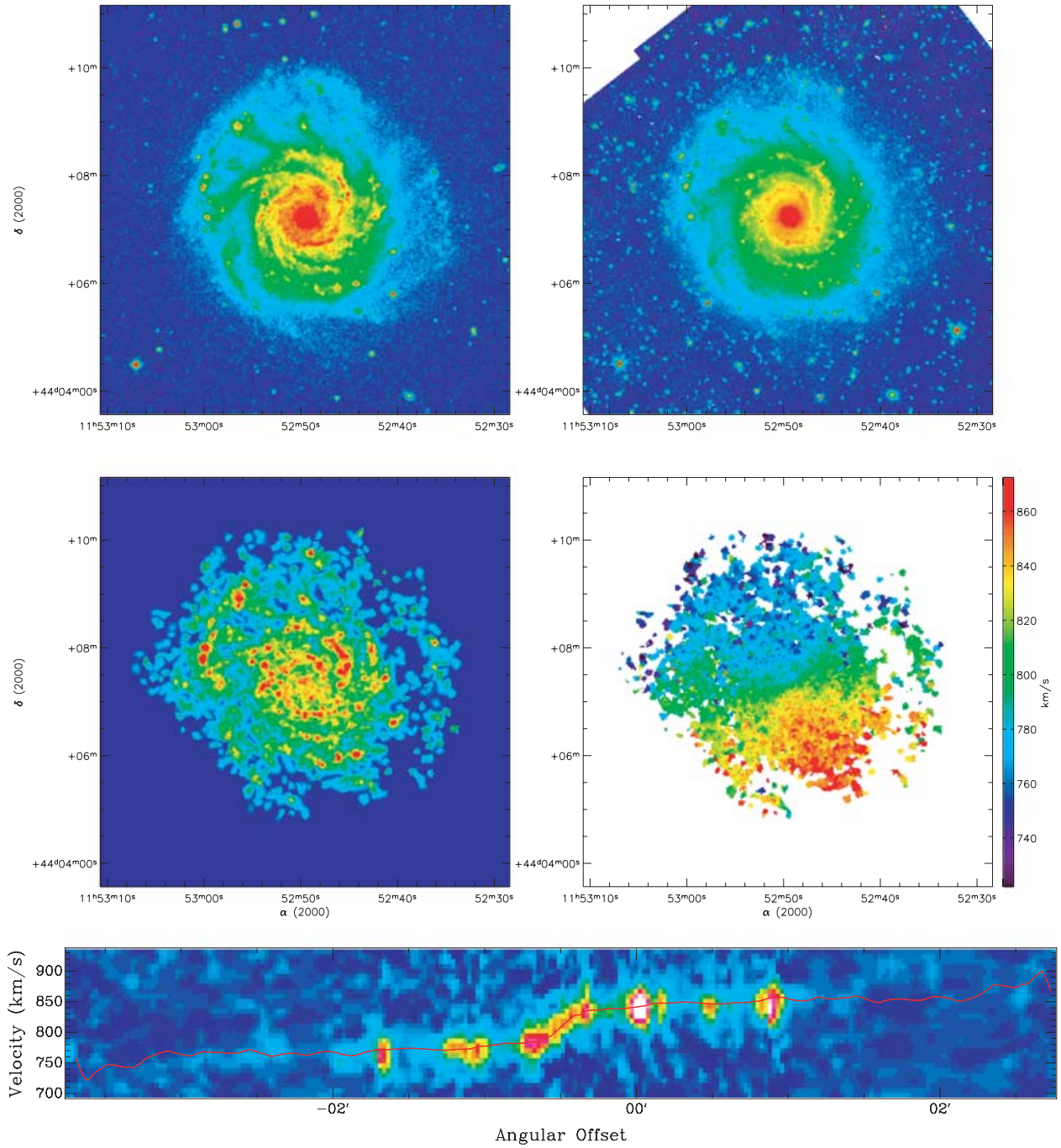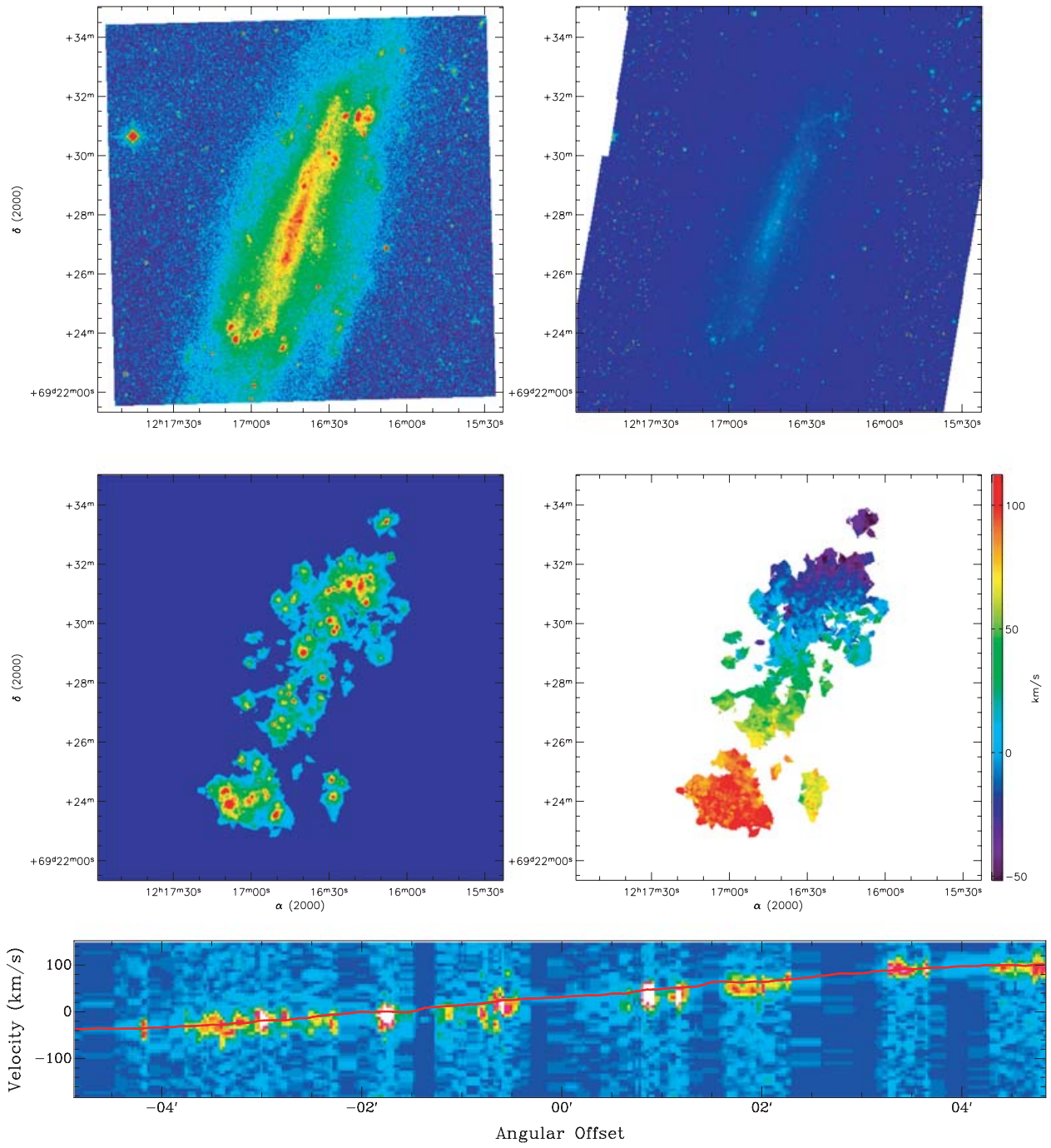
NGC 2403

Figure B3. NGC 2403. Top left: XDSS Blue Band image. Top right: *Spitzer* IRAC 3.6-μm image. Middle left: Hα monochromatic image. Middle right: Hα velocity field. Bottom: PV diagram.

NGC 2798

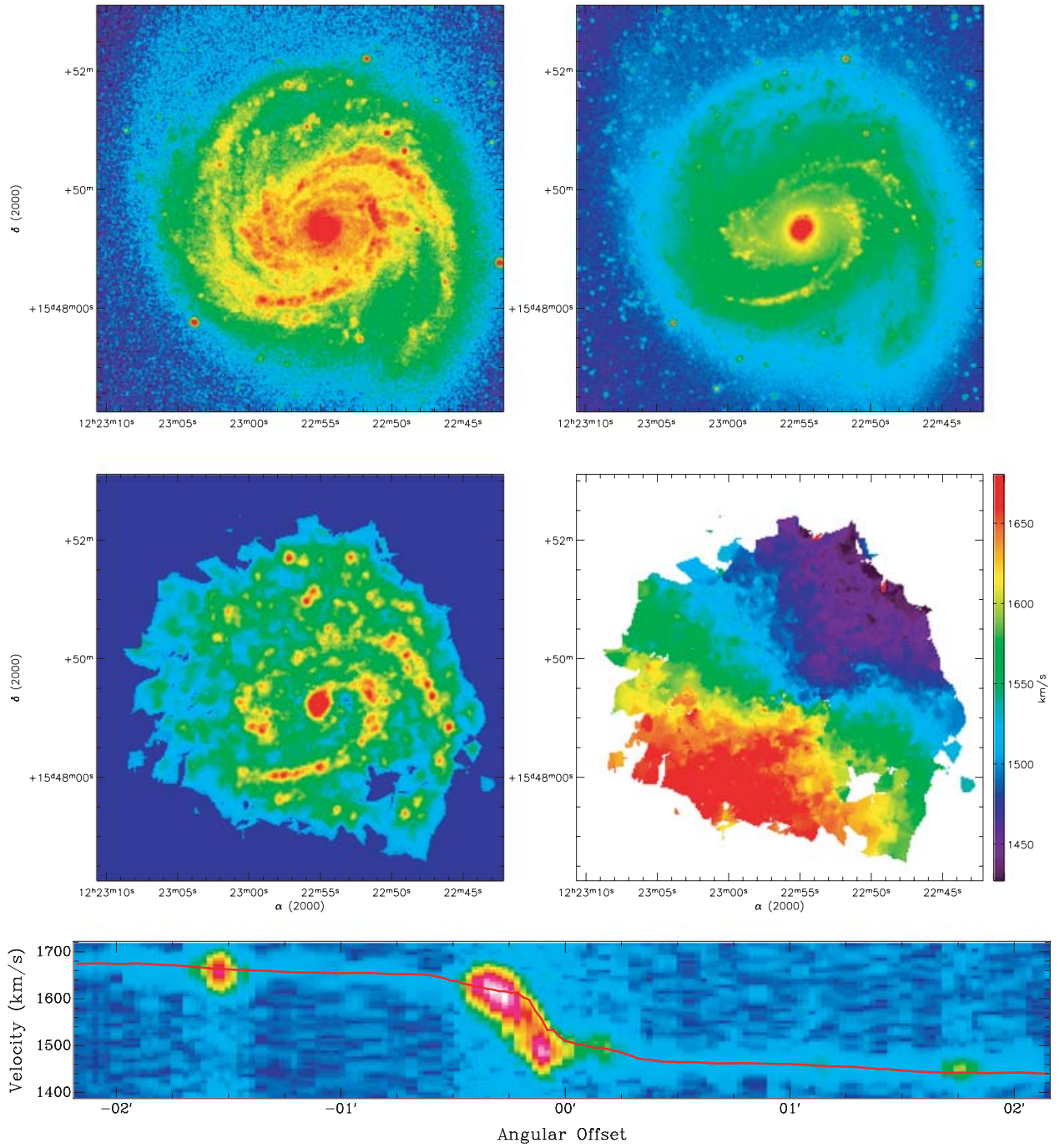**Figure B4.** NGC 2798. Top left: XDSS Blue Band image. Top right: *Spitzer* IRAC 3.6-μm image. Bottom left: Hα monochromatic image. Bottom right: Hα velocity field.

NGC 2915

Figure B5. NGC 2915. Top left: XDSS Blue Band image. Top right: *Spitzer* IRAC 3.6-μm image. Bottom left: Hα monochromatic image. Bottom right: Hα velocity field.

NGC 2976

Figure B6. NGC 2976. Top left: XDSS Blue Band image. Top right: *Spitzer* IRAC 3.6-μm image. Middle left: Hα monochromatic image. Middle right: Hα velocity field. Bottom: PV diagram.
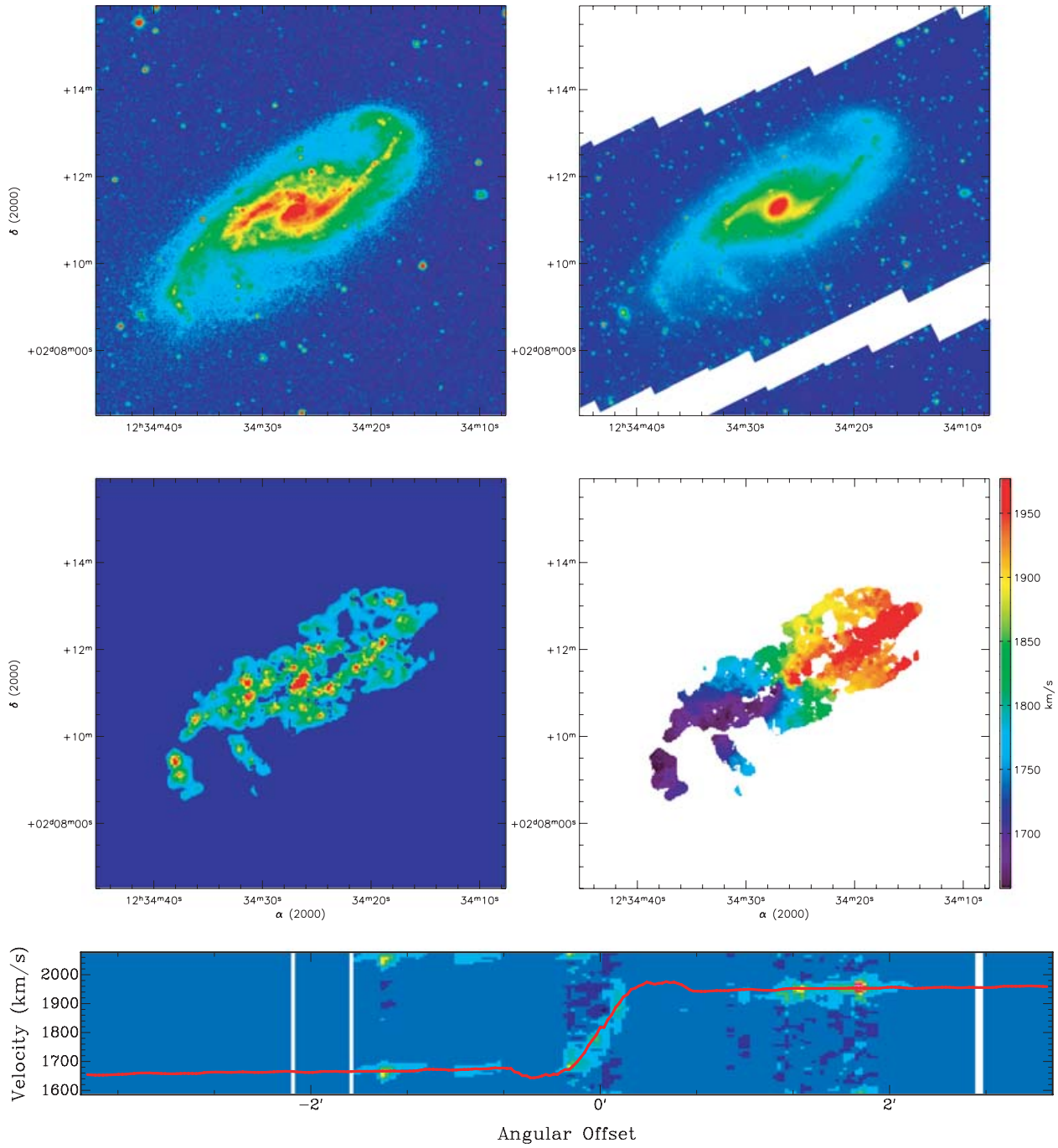
NGC 3031

Figure B7. NGC 3031. Top left: XDSS Blue Band image. Top right: *Spitzer* IRAC 3.6-μm image. Middle left: Hα monochromatic image. Middle right: Hα velocity field. Bottom: PV diagram.
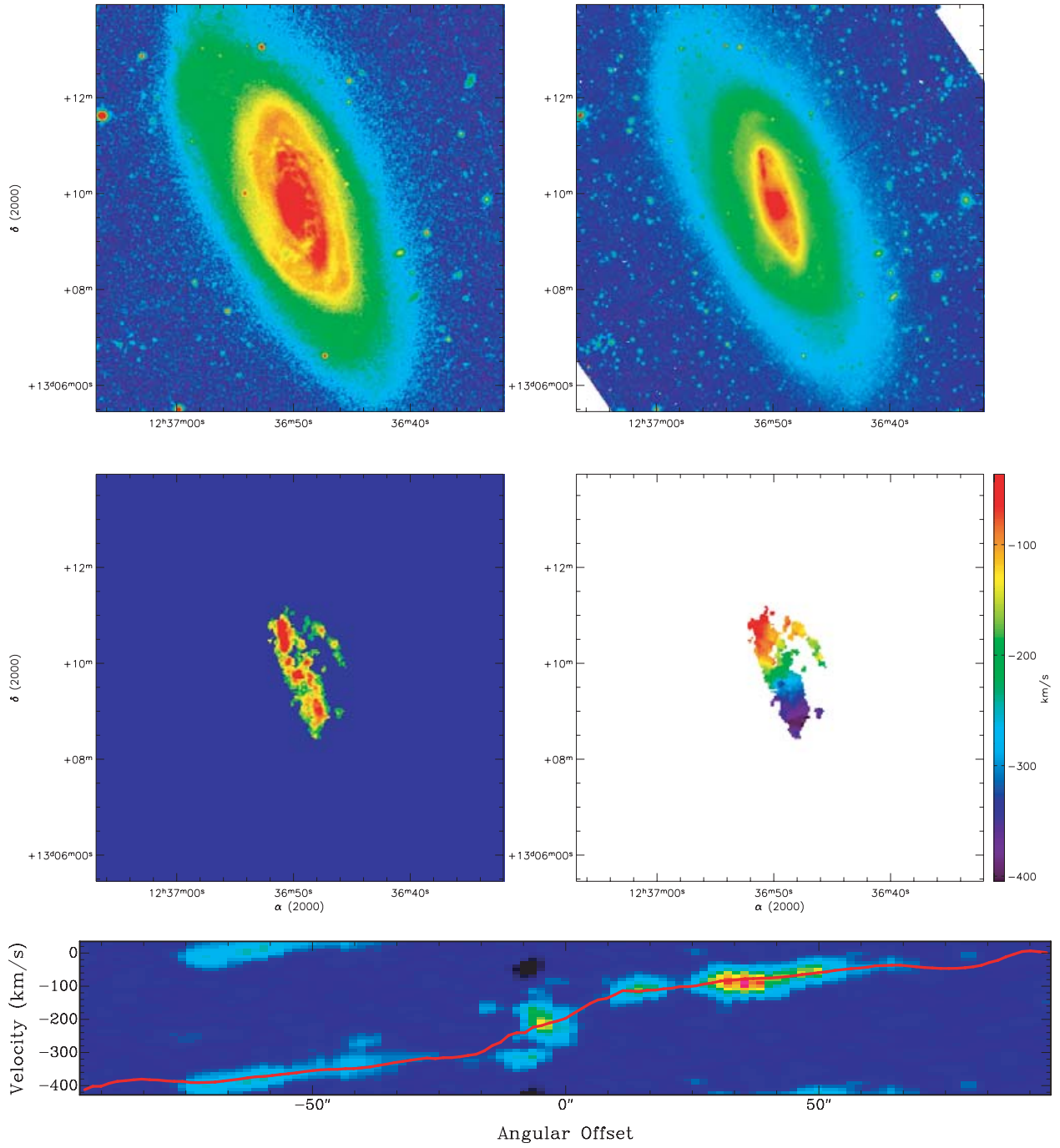
NGC 5423

Figure B8. UGC 5423. Top left: XDSS Blue Band image. Top right: *Spitzer* IRAC 3.6-μm image. Middle left: Hα monochromatic image. Middle right: Hα velocity field. Bottom: PV diagram.

NGC 3049

Figure B9. NGC 3049. Top left: XDSS Blue Band image. Top right: *Spitzer* IRAC 3.6-μm image. Bottom left: Hα monochromatic image. Bottom right: Hα velocity field.

NGC 3184

Figure B10. NGC 3184. Top left: XDSS Blue Band image. Top right: *Spitzer* IRAC 3.6-μm image. Middle left: Hα monochromatic image. Middle right: Hα velocity field. Bottom: PV diagram.

NGC 3198

Figure B11. NGC 3198. Top left: XDSS Blue Band image. Top right: *Spitzer* IRAC 3.6-μm image. Middle left: Hα monochromatic image. Middle right: Hα velocity field. Bottom: PV diagram.
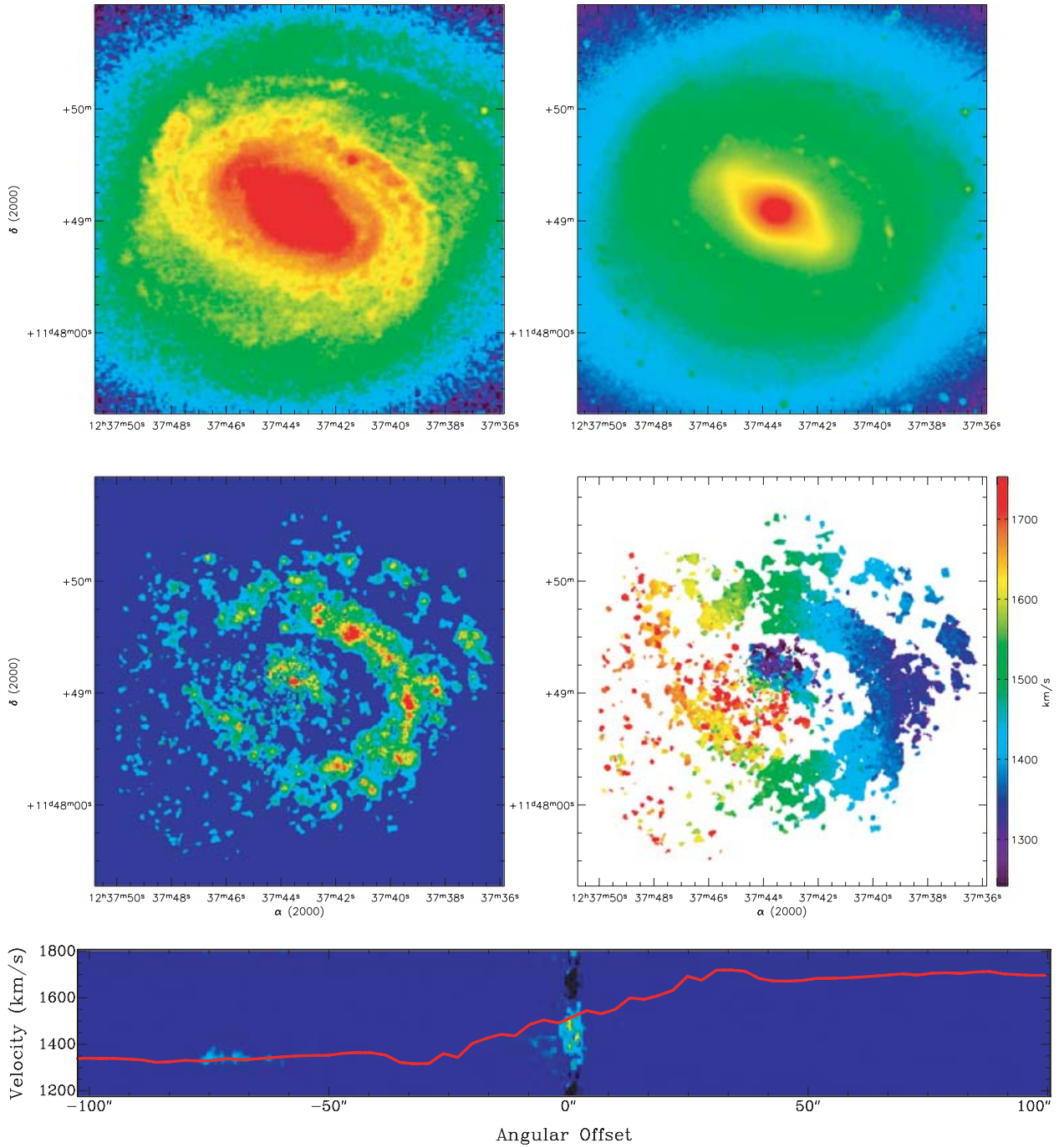
NGC 3521

Figure B12. NGC 3521. Top left: XDSS Blue Band image. Top right: *Spitzer* IRAC 3.6-μm image. Middle left: Hα monochromatic image. Middle right: Hα velocity field. Bottom: PV diagram.
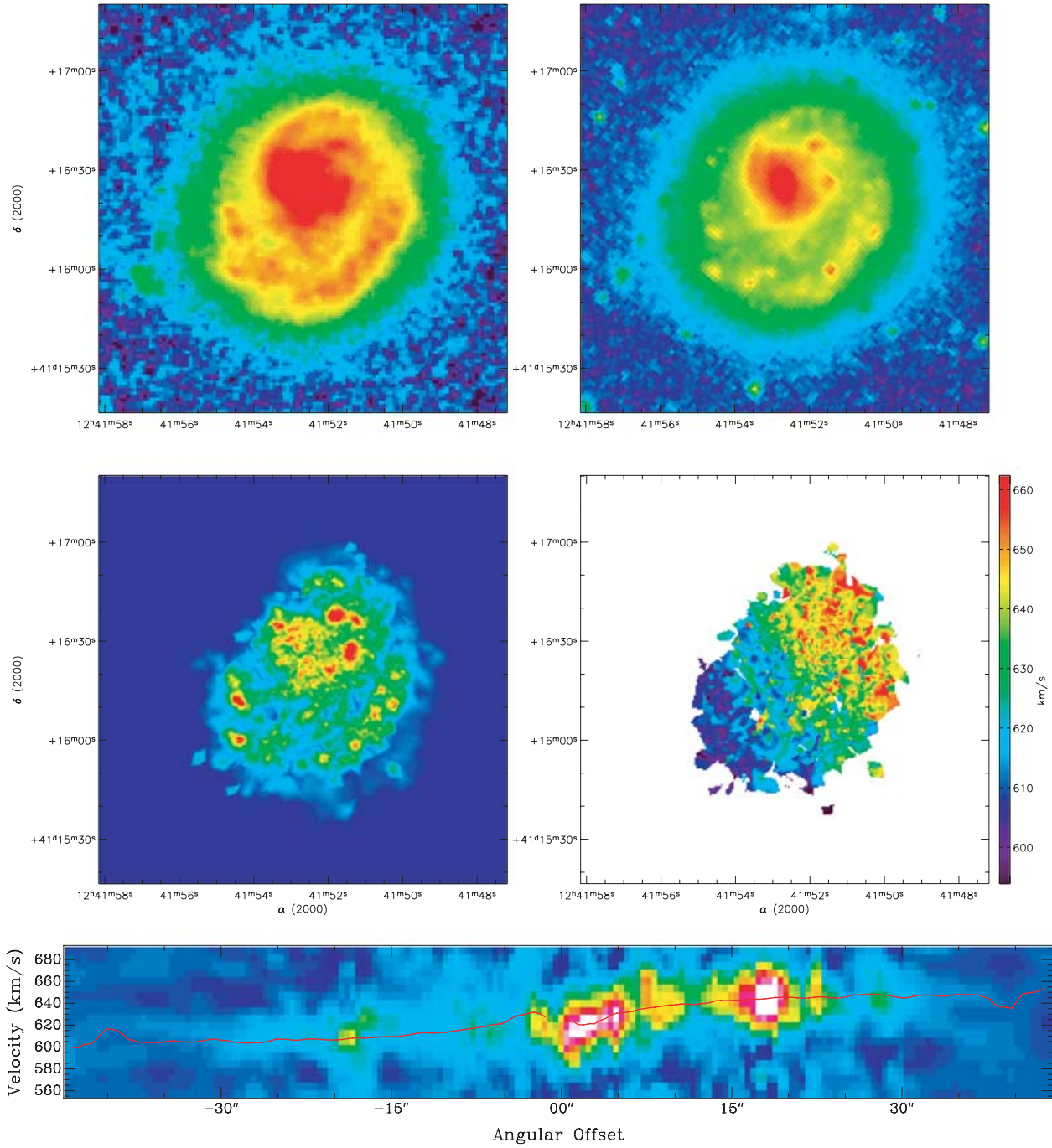
NGC 3621

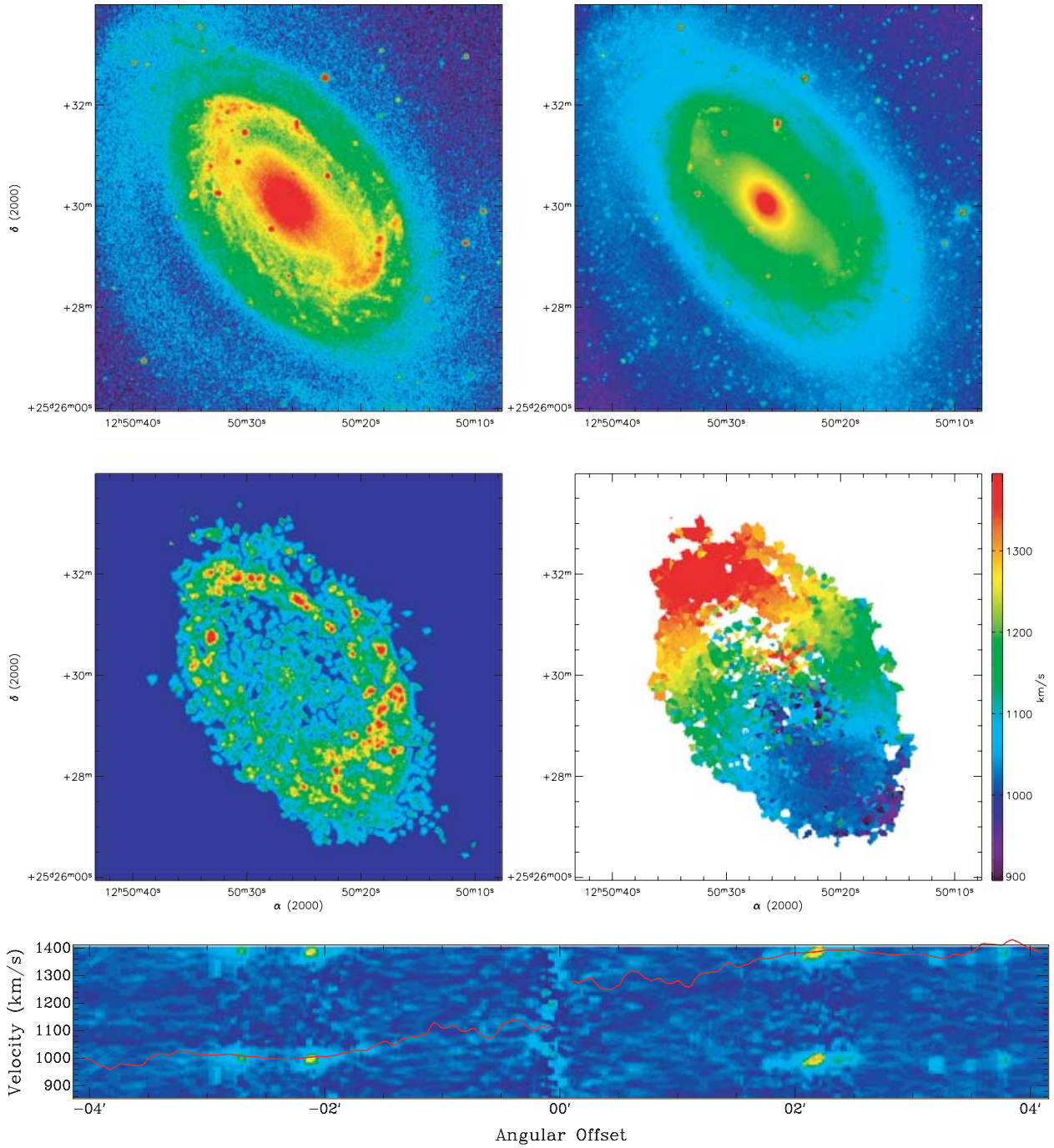**Figure B13.** NGC 3621. Top left: XDSS Blue Band image. Top right: *Spitzer* IRAC 3.6-μm image. Middle left: Hα monochromatic image. Middle right: Hα velocity field. Bottom: PV diagram.

NGC 3938

Figure B14. NGC 3938. Top left: XDSS Blue Band image. Top right: *Spitzer* IRAC 3.6-μm image. Middle left: Hα monochromatic image. Middle right: Hα velocity field. Bottom: PV diagram.

NGC 4236

Figure B15. NGC 4236. Top left: XDSS Blue Band image. Top right: *Spitzer* IRAC 3.6-μm image. Middle left: Hα monochromatic image. Middle right: Hα velocity field. Bottom: PV diagram.
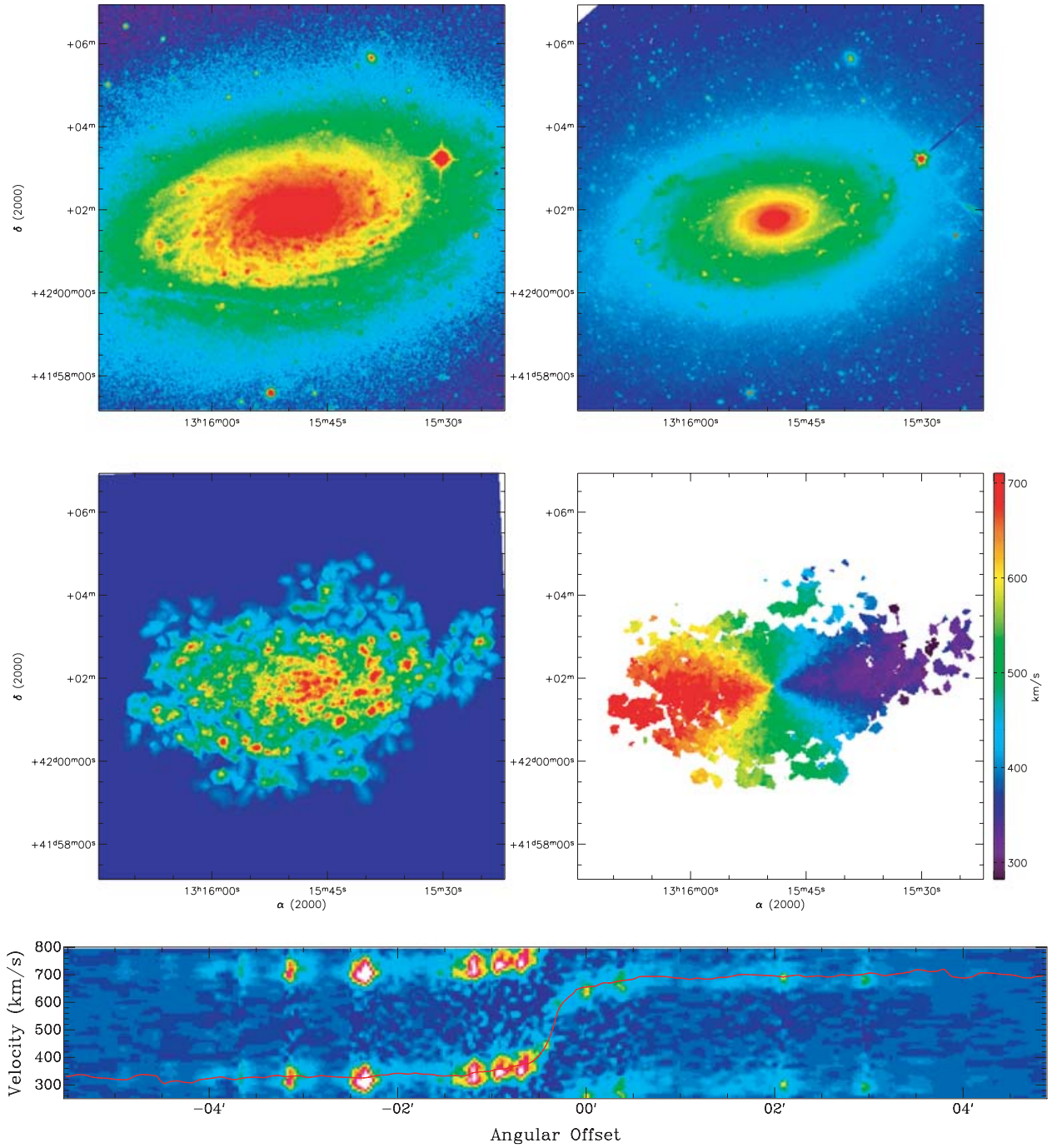
NGC 4321

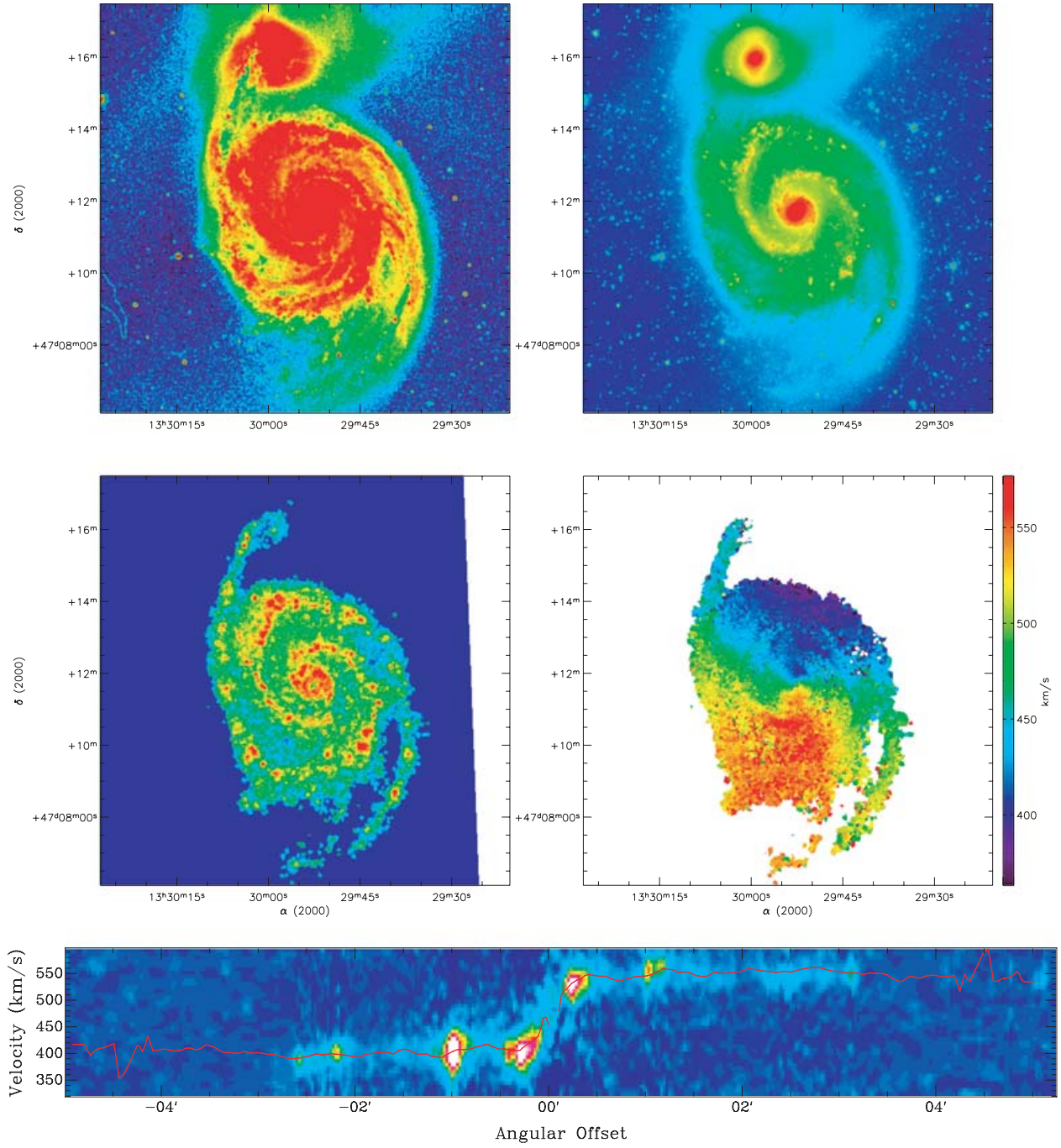**Figure B16.** NGC 4321. Top left: XDSS Blue Band image. Top right: *Spitzer* IRAC 3.6-μm image. Middle left: Hα monochromatic image. Middle right: Hα velocity field. Bottom: PV diagram.

NGC 4536

Figure B17. NGC 4536. Top left: XDSS Blue Band image. Top right: *Spitzer* IRAC 3.6-μm image. Middle left: Hα monochromatic image. Middle right: Hα velocity field. Bottom: PV diagram.

NGC 4569

Figure B18. NGC 4569. Top left: XDSS Blue Band image. Top right: *Spitzer* IRAC 3.6-μm image. Middle left: Hα monochromatic image. Middle right: Hα velocity field. Bottom: PV diagram.

NGC 4579

Figure B19. NGC 4579. Top left: XDSS Blue Band image. Top right: *Spitzer* IRAC 3.6-μm image. Middle left: Hα monochromatic image. Middle right: Hα velocity field. Bottom: PV diagram.
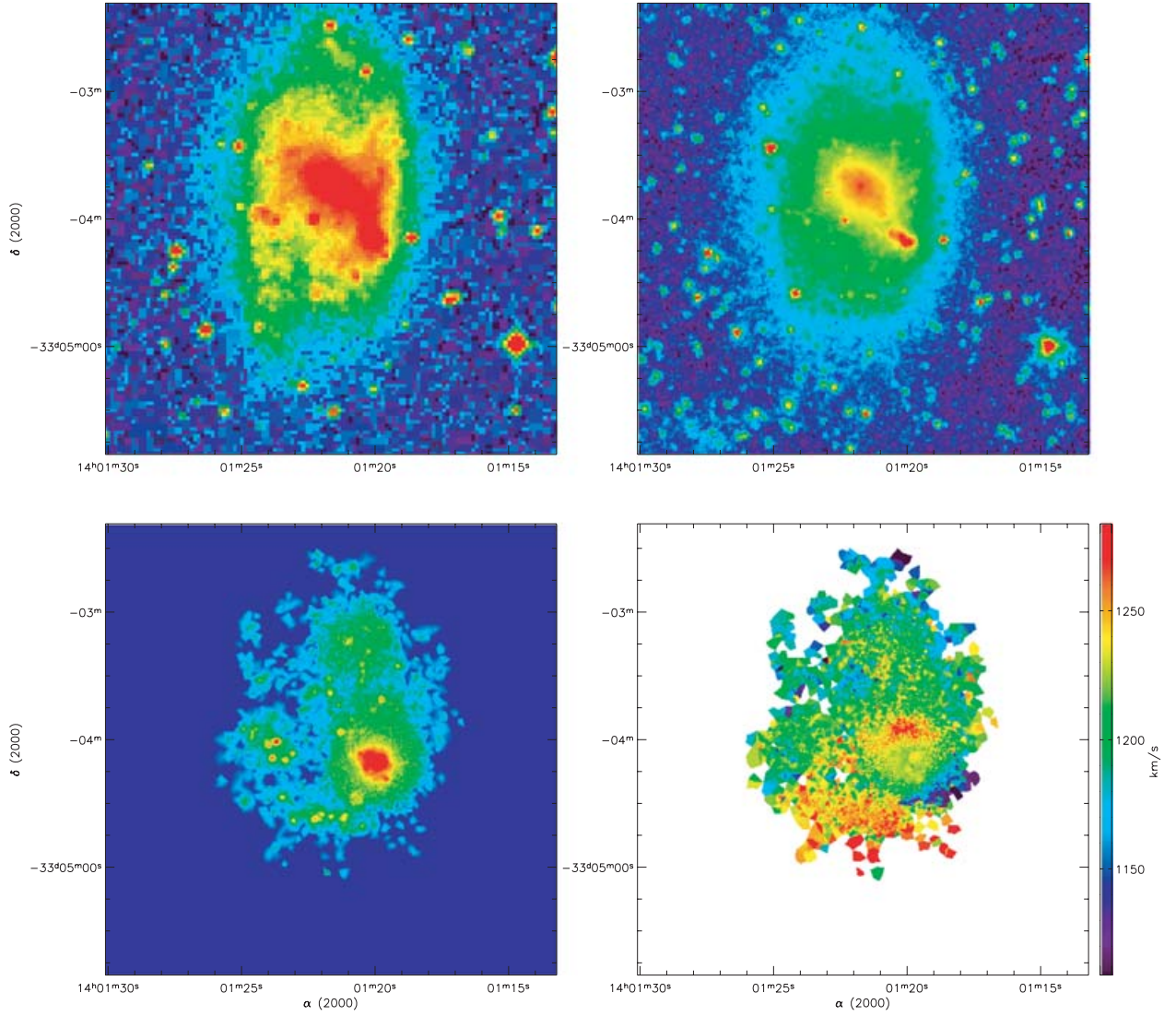
NGC 4625

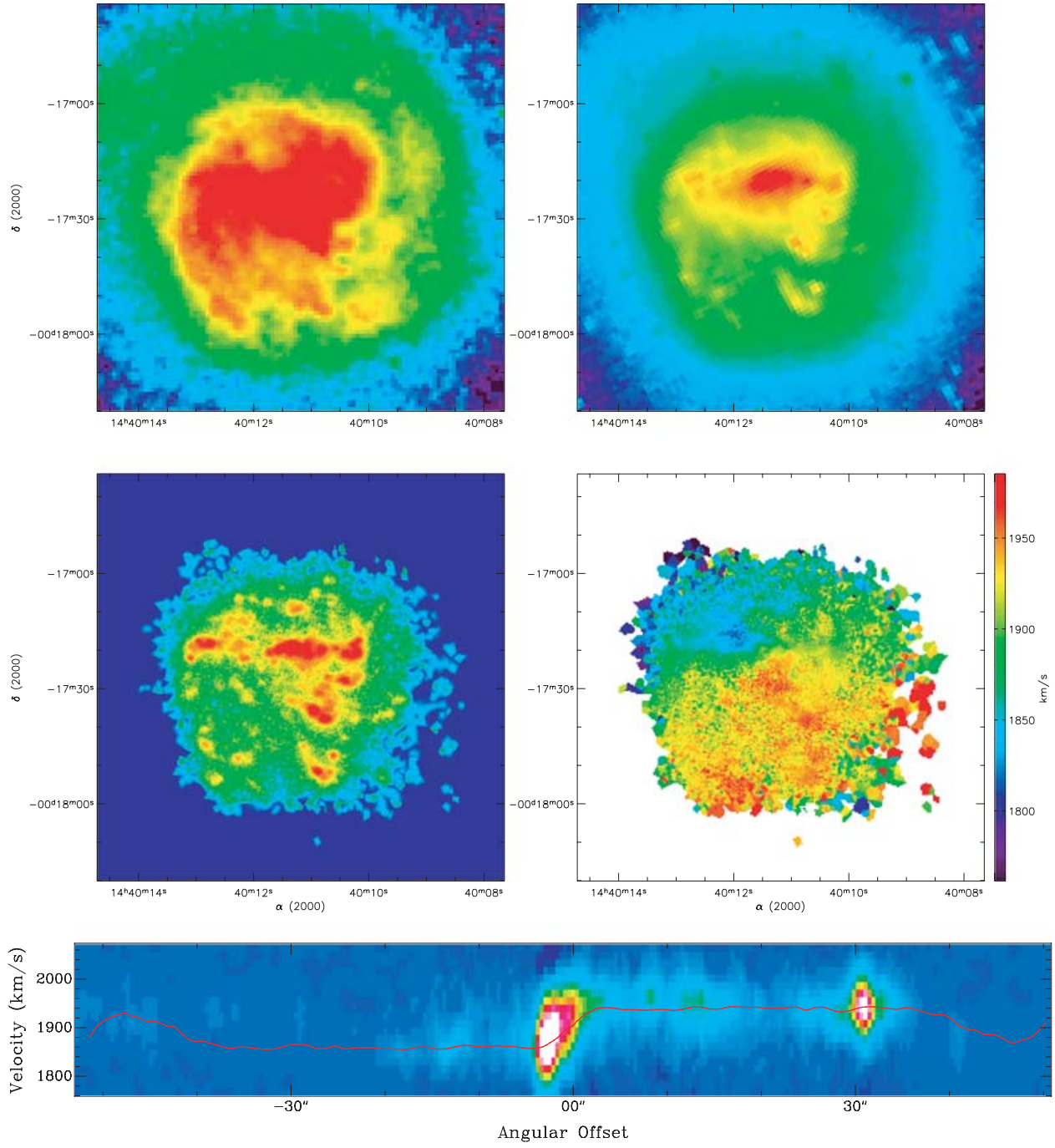**Figure B20.** NGC 4625. Top left: XDSS Blue Band image. Top right: *Spitzer* IRAC 3.6-μm image. Middle left: Hα monochromatic image. Middle right: Hα velocity field. Bottom: PV diagram.

NGC 4725

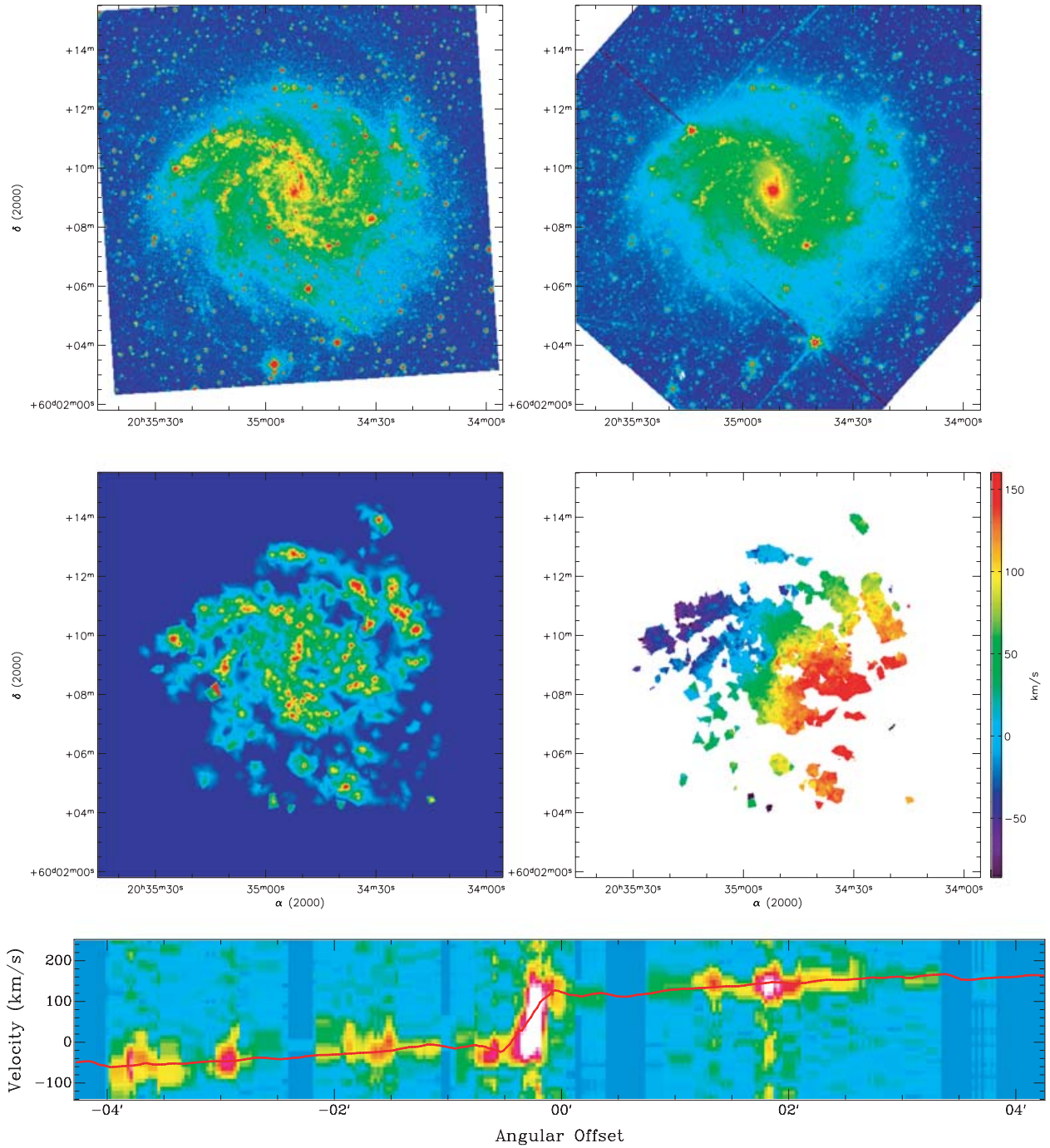**Figure B21.** NGC 4725. Top left: XDSS Blue Band image. Top right: *Spitzer* IRAC 3.6-μm image. Middle left: Hα monochromatic image. Middle right: Hα velocity field. Bottom: PV diagram.

NGC 5055

Figure B22. NGC 5055. Top left: XDSS Blue Band image. Top right: *Spitzer* IRAC 3.6-μm image. Middle left: Hα monochromatic image. Middle right: Hα velocity field. Bottom: PV diagram.

NGC 5194

Figure B23. NGC 5194. Top left: XDSS Blue Band image. Top right: *Spitzer* IRAC 3.6-μm image. Middle left: Hα monochromatic image. Middle right: Hα velocity field. Bottom: PV diagram.
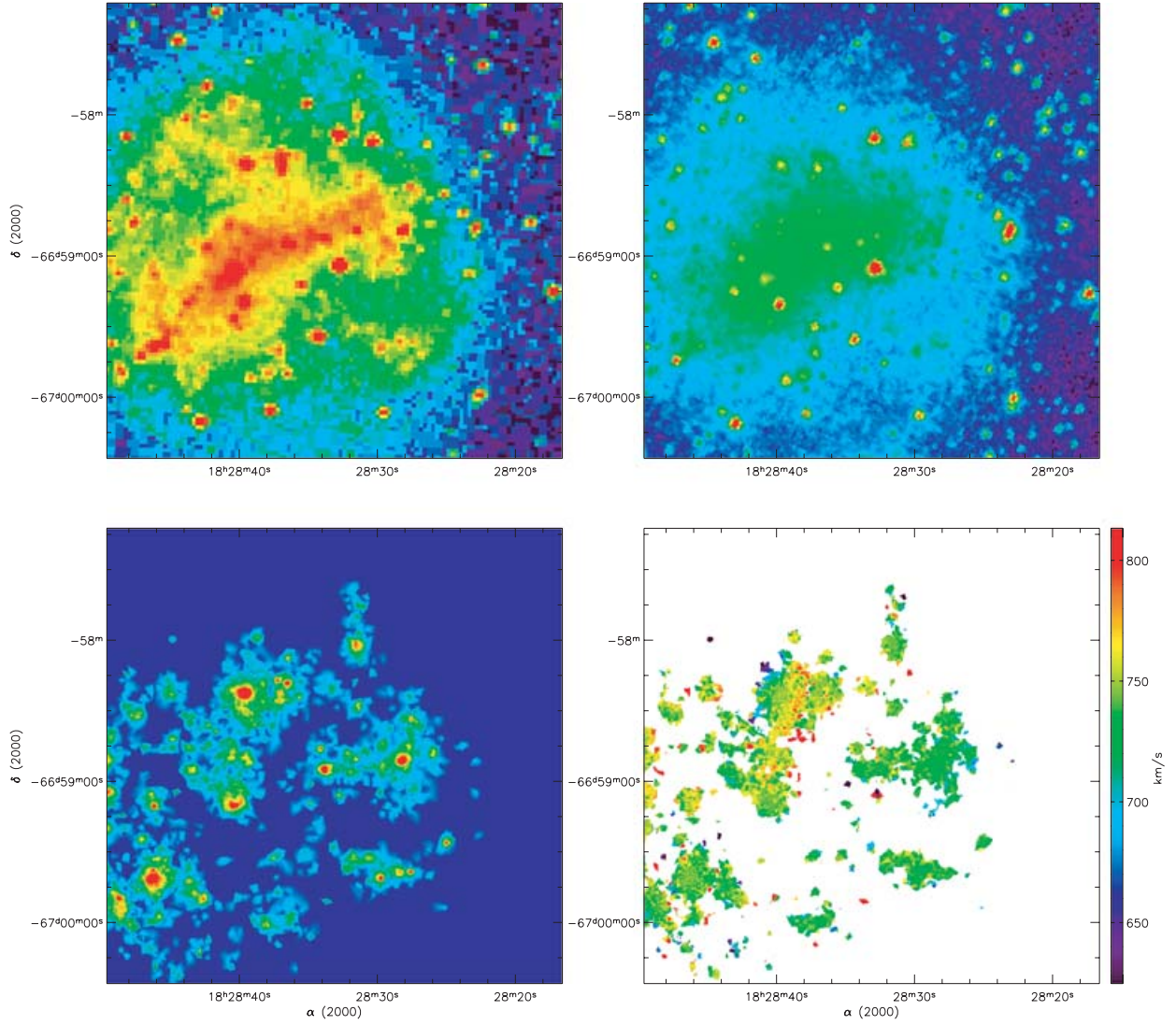
NGC 5398

Figure B24. NGC 5398. Top left: XDSS Blue Band image. Top right: *Spitzer* IRAC 3.6-μm image. Bottom left: Hα monochromatic image. Bottom right: Hα velocity field.
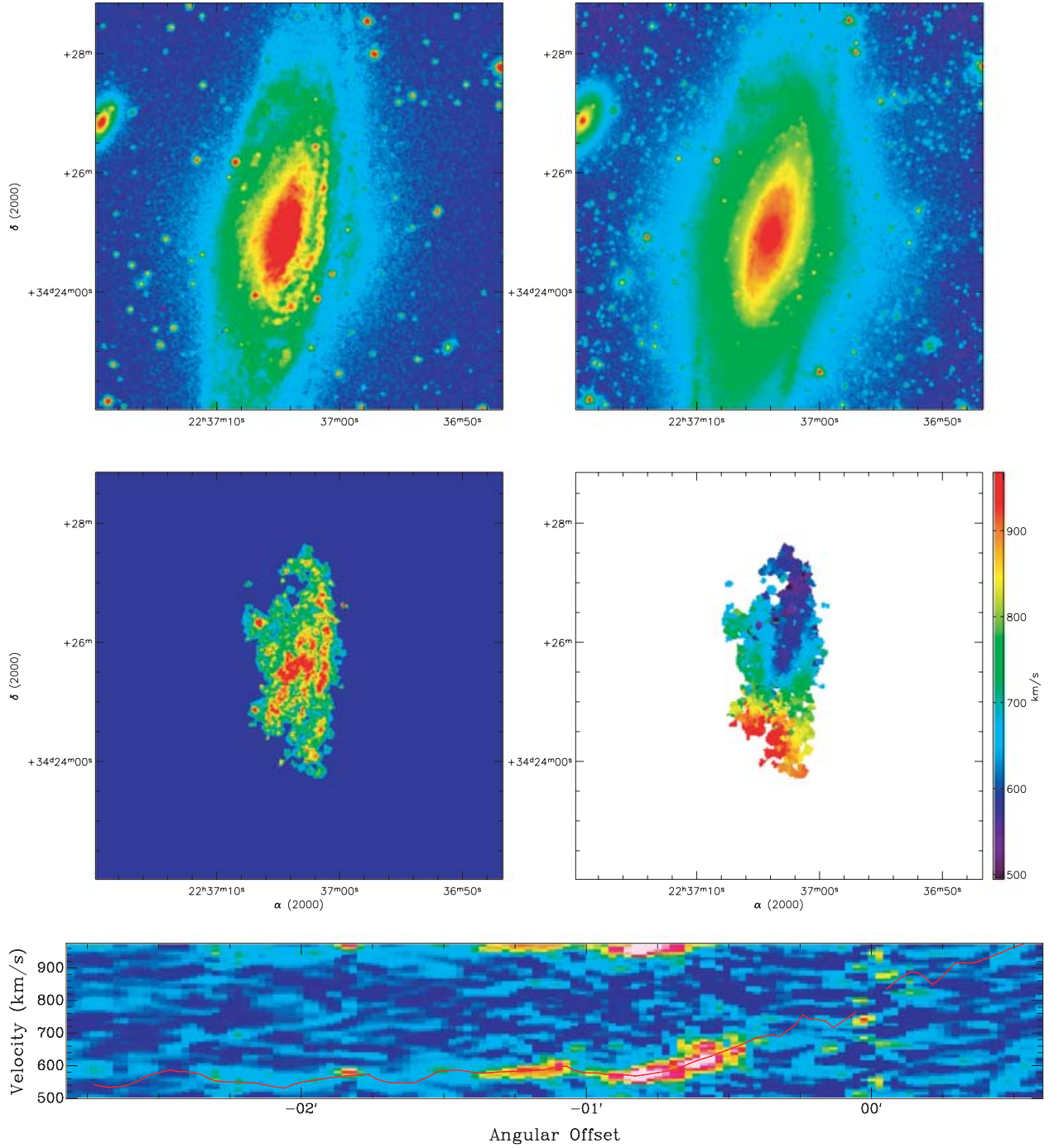
NGC 5713

Figure B25. NGC 5713. Top left: XDSS Blue Band image. Top right: *Spitzer* IRAC 3.6-μm image. Middle left: Hα monochromatic image. Middle right: Hα velocity field. Bottom: PV diagram.

NGC 6946

Figure B26. NGC 6946. Top left: XDSS Blue Band image. Top right: *Spitzer* IRAC 3.6-μm image. Middle left: Hα monochromatic image. Middle right: Hα velocity field. Bottom: PV diagram.

NGC 4710

Figure B27. IC 4710. Top left: XDSS Blue Band image. Top right: *Spitzer* IRAC 3.6-μm image. Bottom left: Hα monochromatic image. Bottom right: Hα velocity field.
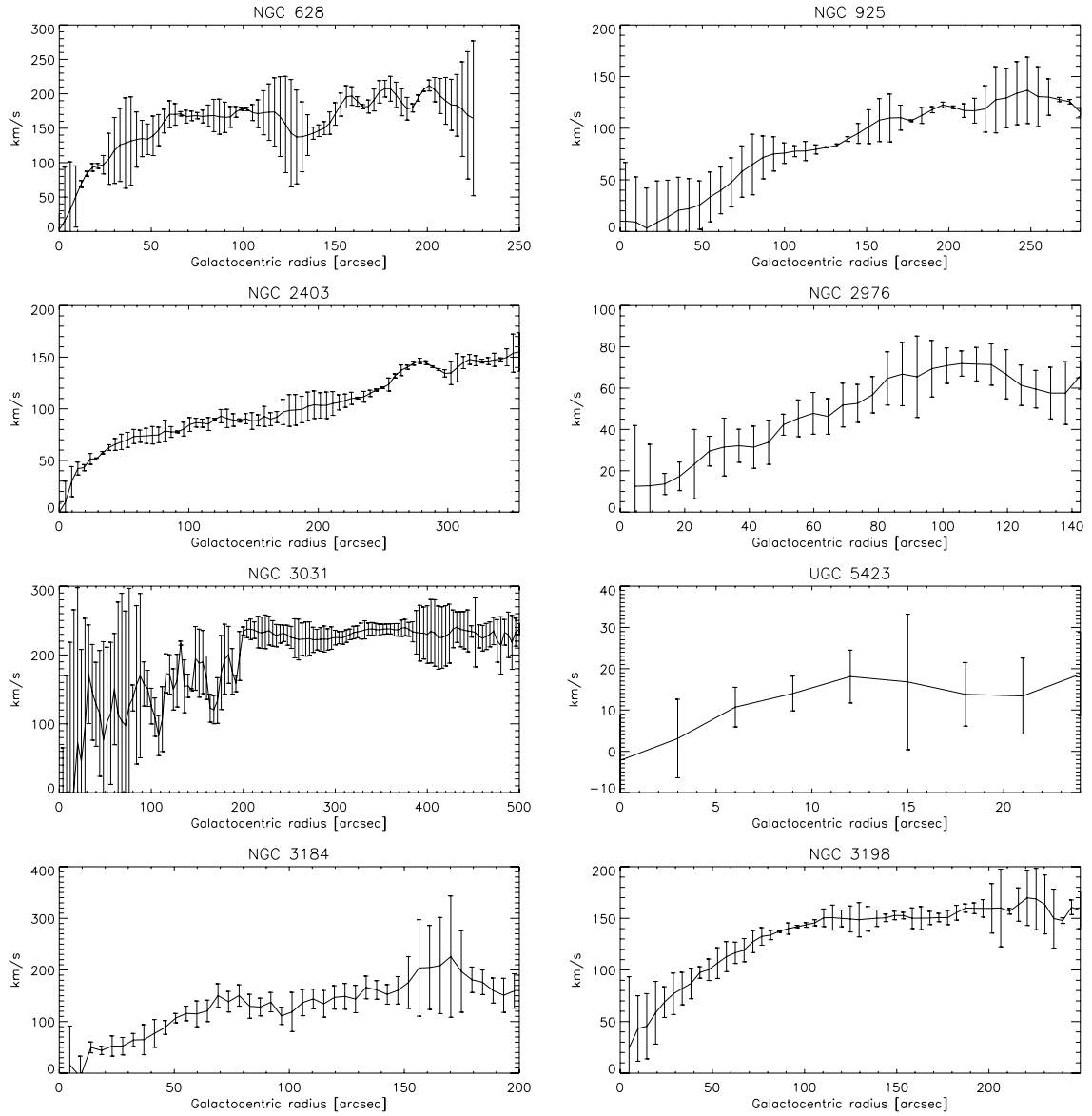
NGC 2403

Figure B28. NGC 7331. Top left: XDSS Blue Band image. Top right: *Spitzer* IRAC 3.6-μm image. Middle left: Hα monochromatic image. Middle right: Hα velocity field. Bottom: PV diagram.

APPENDIX C: ROTATION CURVES

Figure C1. Rotation curves, from top left to bottom right of NGC 628, 925, 2403, 2976, 3031, UGC 5423, NGC 3184 and NGC 3198.
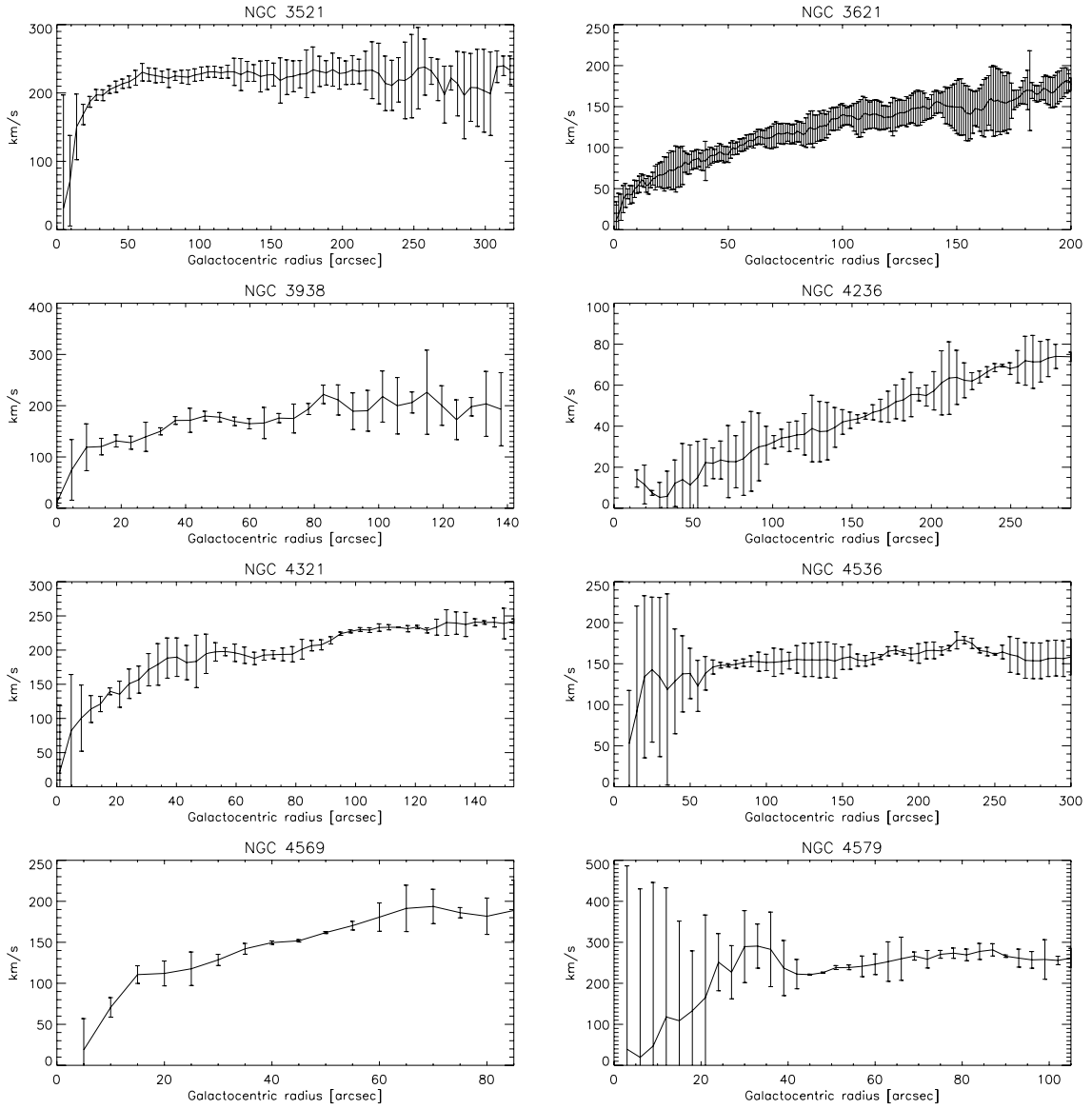
Figure C2. Rotation curves, from top left to bottom right, of NGC 3521, 3621, 3938, 4236, 4321, 4536, 4589 and 4579.
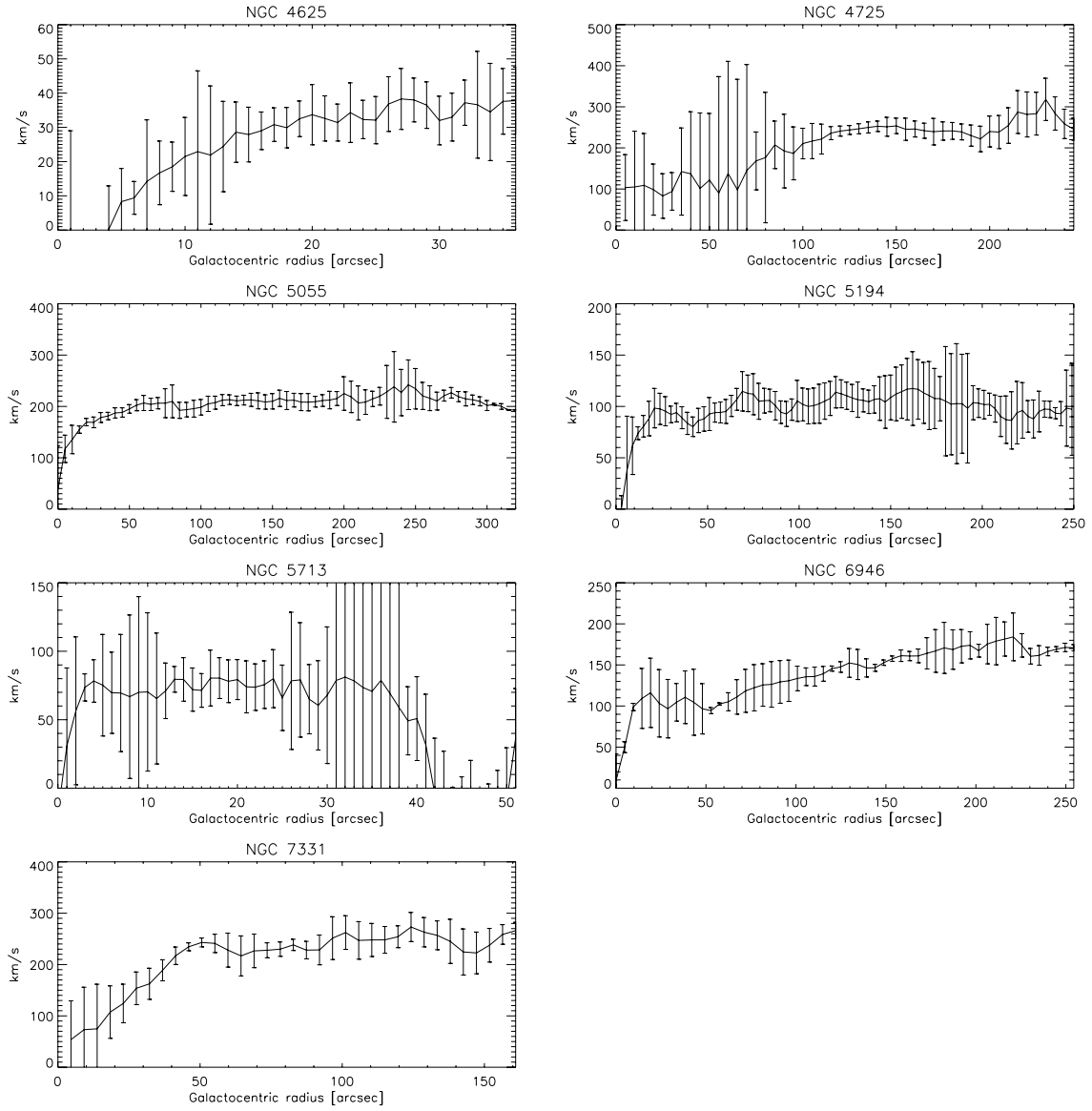
Figure C3. Rotation curves, from top left to bottom right, NGC 4625, 4725, 5055, 5194, 5713, 6946 and 7331.